Dynamics of eddying abyssal mixing layers over rough topography

Henri F. Drake*

Princeton University / Geophysical Fluid Dynamics Laboratory, Princeton, New Jersey, United States

Previously, MIT–WHOI Joint Program in Oceanography/Applied Ocean Science & Engineering, Cambridge and Woods Hole, Massachusetts, United States.

Xiaozhou Ruan

Massachussetts Institute of Technology, Cambridge, Massachusetts, United States

Jörn Callies

California Institute of Technology, Pasadena, California, United States

Kelly Ogden

Western University, London, Ontario, Canada

Andreas M. Thurnherr

Lamont-Doherty Earth Observatory, Palisades, New York, United States

Raffaele Ferrari

Massachussetts Institute of Technology, Cambridge, Massachusetts, United States

**Corresponding author*: Henri F. Drake, henrifdrake@gmail.com

ABSTRACT

The abyssal overturning circulation is thought to be primarily driven by small-scale turbulent mixing. Diagnosed watermass transformations are dominated by rough topography "hotspots", where the bottom-enhancement of mixing causes the diffusive buoyancy flux to diverge, driving widespread downwelling in the interior—only to be overwhelmed by an even stronger upwelling in a thin Bottom Boundary Layer (BBL). These watermass transformations are significantly underestimated by one-dimensional sloping boundary layer solutions, suggesting the importance of three-dimensional physics. Here, we use a hierarchy of models to generalize this one-dimensional boundary layer approach to three-dimensional eddying flows over realistically rough topography. When applied to the Mid-Atlantic Ridge in the Brazil Basin, the idealized simulation results are roughly consistent with available observations. Integral buoyancy budgets isolate the physical processes that contribute to realistically strong BBL upwelling. The downwards diffusion of buoyancy is primarily balanced by upwelling along the canyon flanks and the surrounding abyssal hills. These flows are strengthened by the restratifying effects of submesoscale baroclinic eddies on the canyon flanks and by the blocking of along-ridge thermal wind within the canyon. Major topographic sills block along-thalweg flows from restratifying the canyon trough, resulting in the continual erosion of the trough's stratification. We propose simple modifications to the one-dimensional boundary layer model which approximate each of these three-dimensional effects. These results provide *local* dynamical insights into mixing-driven abyssal overturning, but a complete theory will also require the *non-local* coupling to the basin-scale circulation.

1. Introduction

Below the oceanic pycnocline, the vast volumes of the deep ocean are ventilated by two interconnected cells of a global meridional overturning circulation (Gordon 1986). The lower cell of this circulation is sourced along the coast of Antarctica, where atmospheric cooling and brine rejection transform surface waters into the dense Antarctic Bottom Waters (AABW) that fill the global abyssal ocean at a rate of approximately 30 Sv ($1\,\text{Sv} \equiv 10^6\,\text{m}^3/\text{s}$) (Talley 2013). Since the buoyancy surface bounding AABW from above does not outcrop elsewhere in the ocean, conservation of mass implies that in steady state an equal amount of AABW must upwell across buoyancy surfaces (diabatically) from the abyss. Waters below about 2000 m depth (corresponding to the crests of major topographic features, such as mid-ocean ridges) can upwell diabatically only in the presence of interior watermass transformations (e.g. small-scale turbulent mixing) or fluxes across the seafloor boundary (geothermal heating) (Munk 1966; Walin 1982; Tziperman 1986; Ferrari 2014).

These basic inferences of a global diabatic upwelling from the abyss (e.g. Sverdrup et al. 1942) are also consistent with more detailed inverse modelling at regional scales (e.g. Talley et al. 2003). Most notably, Hogg et al. (1982) consider the fate of 4 Sv of AABW (colder than 0 °C) that enters the Brazil Basin from the Southern Ocean through the Vema Channel; since there are no other exits from the basin and since geothermal fluxes are relatively weak, they infer that turbulent mixing must diffuse heat downward at a rate of $\mathcal{O}(3\,\text{cm}^2/\text{s})$ to balance the upwelling of these waters across the 0 °C isotherm.

Early in-situ turbulence measurements in the upper $\sim$ 1000 m of the interior ocean suggested turbulent diffusivities more than an order of magnitude smaller than those predicted by the large-scale abyssal tracer budgets described above (Gregg 1987; Ledwell et al. 1993).

A subsequent celebrated field campaign in the abyssal waters of the Brazil Basin reported similarly weak background diffusivities over the smooth topography of the abyssal plains, but revealed diffusivities that increased downwards by several orders of magnitude over the rough topography of the Mid-Atlantic Ridge (Polzin et al. 1997; Ledwell et al. 2000). Using regional inverse and forward approaches, respectively, St. Laurent et al. (2001) and Huang and Jin (2002) modelled the impacts of the observed bottom-enhanced mixing on the regional circulation: bottom-enhanced mixing drove interior downwelling while upwelling was restricted to a thin layer of buoyancy convergence near the bottom boundary (as opposed to Munk 1966's uniform upwelling model) and the basin-scale horizontal circulation was dominated by narrow mixing-driven flows along ridge flanks (as opposed to the interior geostrophic flow predicted by Stommel 1958).

The development of mixing parameterizations (e.g. St. Laurent and Garrett 2002; Kunze et al. 2006; Polzin 2009; Melet et al. 2014; de Lavergne et al. 2020) allowed these Brazil Basin results to be generalized to global abyssal watermass transformations (e.g. Nikurashin and Ferrari 2013; de Lavergne et al. 2016; Kunze 2017; Cimoli et al. 2019). Based on such estimates, Ferrari et al. (2016) and McDougall and Ferrari (2017) revised the conceptual model of the global mixing-driven abyssal upwelling: mixing-driven diabatic upwelling is confined to a thin Bottom Boundary Layer (BBL) just above the insulated (or geothermally heated) seafloor, while bottom-enhanced mixing drives diabatic downwelling in the Stratified Mixing Layer (SML) above; the net diabatic overturning is the small remainder of these two large opposing mixing layer flows. In this emerging framework, the global overturning circulation is modulated by the dynamics of thin BBLs (Callies and Ferrari 2018; Drake et al. 2020). Since these abyssal boundary layer flows are challenging to observe (Naveira Garabato et al. 2019; Spingys et al. 2021) and are too thin to be resolved by conventional general circulation models, however, they remain poorly understood (Drake 2021 and Polzin and McDougall 2022 discuss outstanding questions).

The interpretation of the role of boundary mixing in the abyssal overturning circulation (dating back to Munk 1966) has a contentious history: on the one hand, in-situ observations of weakly-stratified bottom mixed layers seemed to imply the existence of vigorous boundary mixing (Armi 1978); on the other hand, it was argued that mixing of already well-mixed waters was inefficient and thus did not lead to significant watermass transformation (see Garrett's 1979 comment and Armi's 1979b reply). Garrett (1990) later formalized his criticism using sloping boundary layer theory (Phillips 1970; Wunsch 1970) and suggested that one-dimensional flows up the sloping bottom boundary—driven by the mixing itself—could provide sufficient restratification to resolve this conundrum. Based on observations of homogeneous layers detached from the bottom boundary (but carrying distinct levels of suspended sediments), Armi (1978, 1979a) instead proposed a three-dimensional boundary–interior exchange process whereby layers are rapidly mixed when they impinge upon topographic features (e.g. seamounts or abyssal hills) and are eventually restratified by along-isopycnal exchanges with the stratified interior.

In light of recent diagnostic evidence for boundary-control on the abyssal circulation (Ferrari et al. 2016), Callies (2018) revisited these ideas to test whether sloping BBL theory is quantitatively consistent with observations. In his analysis of the sloping flank of the Mid-Atlantic Ridge in the Brazil Basin (where co-located measurements of both abyssal mixing rates and stratification are available), he found that the steady state 1D boundary layer solution forced by the observed mixing exhibits a stratification an order of magnitude weaker than observed. The watermass transformations sustained by 1D dynamics alone (Garrett

1990) are thus too inefficient to contribute significantly to the global abyssal overturning circulation.

To reconcile boundary layer dynamics with observations, Callies (2018) argued the stratification of abyssal mixing layers may be maintained by submesoscale baroclinic eddies, which act to slump sloping buoyancy surfaces back to the horizontal. Mixing-driven 1D boundary layer solutions are linearly unstable to submesoscale baroclinic modes (Wenegrat et al. 2018; Callies 2018), in a manner similar to the well-studied analagous problem in the surface mixed layer (Boccaletti et al. 2007; Fox-Kemper et al. 2008). Callies (2018) simulated the finite amplitude evolution of these instabilities in a 3D generalization of the 1D boundary layer framework and showed that the solutions converge on a substantially stronger quasi-equilibrium stratification that is more consistent with observations.

As acknowledged by Callies (2018), however, it is not clear to what extent such idealized solutions are directly applicable to the mid-ocean ridge, which is characterized by particularly rough topography. For example, many of the observations of bottom-enhanced mixing, stratification, and diabatic upwelling from the region are confined to $\mathcal{O}(500\,\mathrm{m})$-deep fracture zone canyons which cut across the ridge (Polzin et al. 1997; Ledwell et al. 2000; St. Laurent et al. 2001; Thurnherr and Speer 2003). To account for these leading-order topographic features, Ruan and Callies (2020) ran simulations of mixing-driven flow over a sinusoidal mid-ocean ridge incised by an idealized Gaussian fracture zone canyon. They confirm Thurnherr and Speer's (2003) speculation that the canyon sidewalls suppress cross-canyon (or along-slope) flow and thus support a vigorous up-canyon (or cross-slope) mean flow. The restratifying tendency of this up-canyon mean flow is much stronger than that of either the 1D up-slope flow or the submesoscale eddies on the smooth ridge flanks, implying that abyssal water-mass transformations are, per unit area, four times larger within the canyons than on the ridge flanks. Ruan and Callies (2020) found, however, that the simulated stratification in the canyon is orders of magnitude larger than observed, suggesting their simulations are still missing important physics. In addition to fracture zone canyons, mid-ocean ridges are also characterized by smaller-scale anisotropic abyssal hills; these features have characteristic scales taller than 1D BBLs and comparable to those of the fastest growing baroclinic mode (Callies 2018; Wenegrat et al. 2018), so we would expect them to affect both mean and eddying circulations. Within the fracture zone canyons, abyssal hills often manifest as sills that substantially block or constrain the deep up-slope flow (Thurnherr et al. 2005; Dell 2013; Dell and Pratt 2015); hydraulic acceleration over the sill produces relatively large velocities also associated with locally enhanced turbulence (Clément et al. 2017).

Here, we use a hierarchy of analytical and numerical solutions to bridge the gap between idealized 1D BBLs and the complexity of observed flows in a region scarred by a fracture zone canyon and dotted with abyssal hills. In Section 2, we review key insights from the 1D BBL buoyancy budget and derive a generalized buoyancy budget that permits topographic variations and spatio-temporal eddy correlations. In Section 3, we describe the "slope-aligned" simulation configuration which leverages a coordinate frame aligned with the mean topographic slope to allow restratification by mean up-slope flow across a uniform background vertical buoyancy gradient. In Section 4, we describe the simulated mixing layer flows in a simulation with realistic topography and show they are qualitatively consistent with available observations. In Section 5, we present simulated buoyancy budgets, and show a balance between bottom-enhanced mixing, submesoscale eddy fluxes, and the cross-slope mean flow. By progressively simplifying the configuration in a hierarchy of models framework (Held 2005), we isolate the roles of individual physical processes in setting the near-boundary stratification. In Section 6, we discuss how our results bridge the gap between interpretations of in-situ observations (e.g. Armi 1978; Thurnherr and Speer 2003; Thurnherr et al. 2020) and 1D BBL theory (e.g. Garrett 1979; Garrett et al. 1993), and how they illustrate—at a regional scale—the control of abyssal mixing layers on an "upside-down" abyssal overturning circulation (Ferrari et al. 2016). We conclude that a combination of mixing-driven up-slope flows, submesoscale baroclinic eddies, and topographic control are required to maintain a steady state near-boundary stratification consistent with in-situ observations and a finite global abyssal overturning circulation.

2. Theory

We review the derivation and results of sloping boundary layer theory in Sections 2a,b in anticipation of our generalization to three-dimensional flows over rough sloping topography in Section 2c.

a. Slope-aligned equations

In sloping boundary layer theory (Wunsch 1970; Phillips 1970; Garrett et al. 1993; Thompson and Johnson 1996; Callies 2018; Holmes and McDougall 2020), analytical progress is achieved by modelling the system in a coordinate frame aligned with its mean topographic slope, rather than the typical coordinate frame $(\hat{x}, \hat{y}, \hat{z})$ with $\hat{z}$ aligned with gravity. It is useful to decompose the buoyancy $B = N^2\hat{z} + b$ into a background component $N^2\hat{z}$, where N^2 is a constant vertical buoyancy gradient, and a perturbation component $b(\hat{x}, \hat{y}, \hat{z}, t)$; the background buoyancy is assumed to be in hydrostatic balance with a background pressure and we similarly decompose $P = \frac{1}{2}N^2\hat{z}^2 + p$. Then, we rotate the coordinate system to a coordinate frame aligned with the mean-slope $(x, y, z) \equiv (\hat{x}\cos\theta + \hat{z}\sin\theta, \hat{y}, \hat{z}\cos\theta - \hat{x}\sin\theta)$, where θ is the region's average slope angle in the $\hat{x}$-direction (e.g. dashed black lines in Figure 3b). For small slopes[1] $\tan\theta \ll 1$, the hydrostatic Boussinesq equations in the mean-slope coordinates are, at leading order, given by

$$u_t + \mathbf{u}\cdot\nabla u - fv\cos\theta = -p_x + b\sin\theta + \nabla\cdot(\nu\nabla u)\,, \tag{1}$$

$$v_t + \mathbf{u}\cdot\nabla v + fu\cos\theta = -p_y + \nabla\cdot(\nu\nabla v)\,, \tag{2}$$

$$p_z = b\cos\theta, \tag{3}$$

$$\nabla\cdot\mathbf{u} = 0, \tag{4}$$

$$b_t + \mathbf{u}\cdot\nabla b + N^2(w\cos\theta + u\sin\theta) = \nabla\cdot\left[\kappa\left(N^2\cos\theta\mathbf{z} + \nabla b\right)\right]\,, \tag{5}$$

where subscripts represent partial derivatives, ∇ is the gradient operator, u is the along-canyon (or cross-slope) velocity, v is the cross-canyon (or along-slope) velocity, w is the slope-normal velocity, f is a constant Coriolis parameter, κ is an isotropic eddy diffusivity, and $\nu = \sigma\kappa$ is an isotropic eddy viscosity determined by the turbulent Prandtl number σ. The rotated along-canyon $\mathbf{x}$-momentum equation is identical in form to the zonal $\hat{\mathbf{x}}$-momentum equation with the exception of the small but dynamically significant projection of the perturbation buoyancy force $b\hat{\mathbf{z}}$ on $\mathbf{x}$.

The anomalous seafloor depth, relative to the mean slope, is given by

$$d(x, y) = \hat{d}(\hat{x}, \hat{y}) + \hat{x}\tan\theta \tag{6}$$

We set $z = 0$ along the sloping plane that intersects the point with the greatest anomalous seafloor depth, $\max(d)$ (see Figure 2). Boundary conditions at the seafloor, $z = \max(d) -$

[1]While $\sin\theta \simeq \theta$ and $\cos\theta \simeq 1$ in this limit, we retain these geometric terms explicitly so they are not forgotten.

$d(x, y)$, are $\mathbf{u} = 0$ (no-slip[2] and no-normal-flow) and $\mathbf{n} \cdot (\kappa \nabla B) = 0$ (insulating[3]), where $\mathbf{n}$ is a unit vector normal to the boundary.

b. Smooth planar slopes and steady 1D dynamics

Assuming a constant topographic slope ($d \equiv 0$) and mixing rates that vary only in the slope-normal direction, the equilibrium solution reduces to

$$-fv\cos\theta = b\sin\theta + \partial_z\left(\nu u_z\right), \tag{7}$$

$$fu\cos\theta = \partial_z\left(\nu v_z\right), \tag{8}$$

$$p_z = b\cos\theta, \tag{9}$$

$$uN^2\sin\theta = \partial_z\left[\kappa\left(N^2\cos\theta + b_z\right)\right], \tag{10}$$

where the continuity equation $w_z = 0$ combines with the no-normal-flow bottom boundary condition at $z = 0$ to require $w \equiv 0$ everywhere (no slope-normal exchange). These equations can be solved analytically in the case of constant parameter values (Wunsch 1970; Phillips 1970; Thorpe 1987; Garrett 1990), or approximately for varying parameters in some asymptotic limits (Salmun et al. 1991; Callies 2018). In either case, the slope Burger number $S \equiv N^2\tan^2\theta/f^2$ and the BBL thickness

$$\delta \equiv q^{-1} = \sqrt{\frac{2\nu}{f}}\left(1 + S\sigma\right)^{-\frac{1}{4}}, \tag{11}$$

emerge as key parameters. We recognize δ as the Ekman layer thickness $\delta_E \equiv \sqrt{\frac{2\nu}{f}}$, modified by buoyancy effects at the sloping boundary; for typical abyssal values, $S \ll 1$ and $\sigma = \mathcal{O}(1)$ such that buoyancy effects are weak (Thurnherr and Speer 2003).

---

[2] While applying a bottom drag to match the unresolved Reynolds' stresses in the turbulent log-layer would be a more defensible option (Taylor and Shaw 1920), we choose the no-slip condition for a closer correspondence to 1D BBL models.

[3] Geothermal heating is thought to contribute negligibly to abyssal watermass transformations in the BBTRE canyon region (Thurnherr et al. 2020), so we ignore it for simplicity here.

Recalling the crucial assumption of a constant background vertical stratification N^2, the slope-aligned buoyancy equation (10) describes a direct balance between slope-normal diffusion of heat downwards towards the boundary and cross-slope advection against the constant background buoyancy gradient; this balance is a near-boundary analog of Munk's (1966) classic interior ocean vertical balance. This is best illustrated by integrating (10) in the slope-normal direction,

$$\psi(z) \equiv \int_0^z u \, \mathrm{d}z = \kappa \cot\theta \left(B_z/N^2 \cos\theta\right) = \kappa \cot\theta \left(1 + b_z/N^2 \cos\theta\right), \tag{12}$$

where ψ is the up-slope transport (per along-slope unit length) and we have invoked the insulating bottom boundary condition on the full stratification, $B_z = 0$ at $z = 0$.

Consider the case of exponentially bottom-enhanced mixing, $\kappa(z) = \kappa_{\mathrm{BG}} + \kappa_{\mathrm{BOT}}\, e^{-z/h}$ with $\kappa_{\mathrm{BOT}}/\kappa_{\mathrm{BG}} \gg 1$. Equation (12) reveals two keys insights:

1. The net up-slope transport, integrated over both the upwelling BBL and the downwelling SML, converges to the negligibly small value[4]

$$\psi_\infty \equiv \psi(z \to \infty) = \kappa_{\mathrm{BG}} \cot\theta \qquad \text{(the 1D integral constraint)} \tag{13}$$

since far from the boundary $b_z \to 0$ (Thorpe 1987) and both $\kappa(z) \to \kappa_{\mathrm{BG}}$ and $\cot\theta$ are small.

2. Maximal up-slope transport in the BBL is achieved when both κ is large (i.e. near the boundary) and B_z is large (strong restratification). If the stratification is maintained near the background value $N^2 \cos\theta$ where the diffusivity is large (i.e. $z \ll h$) then the up-slope transport in the BBL reaches an upper bound $\max\{\psi\} \simeq \kappa_{\mathrm{BOT}} \cot\theta = \frac{\kappa_{\mathrm{BOT}}}{\kappa_{\mathrm{BG}}}\psi_\infty \gg \psi_\infty$.

[4]While $\psi_\infty \to \infty$ as $\theta \to 0$, the adjustment timescales also grows, $\tau_{\mathrm{BBL}} = \delta^2/\kappa_{\mathrm{BG}} \propto \cot\theta \to \infty$, making it more likely that other dynamics disrupt the approach to equilibrium.

Callies (2018) derives approximate but analytical boundary layer solutions to the steady 1D system (eqs. 7–10) for bottom-enhanced mixing. In the abyssal ocean regime with typical values of $S\sigma \ll 1$, the equilibrium stratification B_z is approximately inversely proportional to κ in the SML (their eq. 10; Figure 1a, solid lines), such that the diffusive buoyancy flux $\kappa B_z \simeq \kappa_{\text{BG}} N^2 \cos\theta$ is constant and finite buoyancy flux convergence occurs only within the thin BBL. Since the BBL stratification is reduced to roughly $B_z \approx \frac{\kappa_{\text{BG}}}{\kappa_{\text{BOT}}} N^2 \cos\theta$ (Figure 1a, solid lines) and near-boundary mixing is thus inefficient, up-slope BBL transport is roughly equal to the negligibly small integral constraint (13), $\max\{\psi\} \simeq \kappa_{\text{BG}} \cot\theta$ (Figure 8a, dotted and dashed lines). This weak BBL upwelling and negligible SML downwelling contrasts with the strong bi-directional flows inferred from watermass transformation analyses (Ferrari et al. 2016; McDougall and Ferrari 2017).

c. Rough topography and eddy fluxes

We now derive the 3D BBL buoyancy budget, which allows for topographic and flow variations along the plane of the slope. Consider the buoyancy budget for a volume $\mathcal{V}$ within a height z above the mean slope (Figure 2):

$$\iiint_{\mathcal{V}(z'<z)} b_t \, \mathrm{d}V = \iint_{\mathcal{A} \equiv \partial\mathcal{V}(z'<z)} (-\mathbf{u}B + \kappa\nabla B) \cdot \mathbf{n} \, \mathrm{d}A, \tag{14}$$

where we use the divergence theorem to rewrite the right-hand side terms in terms of fluxes normal to the bounding surface $\partial\mathcal{V}$ (Figure 2). Fluxes through the seafloor at $z' = \max(d) - d(x, y)$ vanish due to the no-flow and insulating bottom boundary conditions. Motivated by the simulations in Section 3, we assume fluxes through cross-slope and along-slope boundaries cancel due to periodicity (e.g. $b(x) = b(x + L_x)$), except for the up-slope flow across the background buoyancy gradient (recall $B = N^2\hat{z} + b$),

$$\iint_{\mathcal{A}(x+L_x;\, z'\leq z)} (-uB)\ \mathrm{d}y\mathrm{d}z' - \iint_{\mathcal{A}(x;\, z'\leq z)} (-uB)\ \mathrm{d}y\mathrm{d}z' = -N^2 L_x \sin\theta \iint_{\mathcal{A}(x;\, z'\leq z)} u\,\mathrm{d}y\mathrm{d}z' \tag{15}$$

This, combined with the slope-normal component of the flux through the $z' = z$ surface, gives

$$\underbrace{\iiint_{\mathcal{V}(z'\leq z)} b_t\,\mathrm{d}V}_{\text{LHS}} = \underbrace{\underbrace{-\langle -\kappa B_z\rangle}_{\text{Mixing}} \underbrace{-\langle wb\rangle}_{\text{Eddies}} \underbrace{-N^2 L_x \sin\theta\Psi}_{\text{Mean Flow}}}_{\text{RHS}}, \tag{16}$$

where we define $\langle\,\phi\,\rangle \equiv \iint_{\mathcal{A}(z)} \phi\,\mathrm{d}x\mathrm{d}y$ as the slope-integral operation and $\Psi(z) \equiv \iint_{\mathcal{A}(x;\, z'\leq z)} u\,\mathrm{d}y\mathrm{d}z'$ as the up-slope transport across the periodic boundary (Figure 2a). At equilibrium, the form of the generalized volume-integral buoyancy equation (16) is similar to the 1D transport equation (12), although there is now an additional eddy flux of buoyancy towards or away from the boundary, and the turbulent buoyancy flux may be modified by along- and cross-slope correlations between κ and B_z. Assuming a steady state and integrating up far into the interior, where $\kappa \to \kappa_{\mathrm{BG}}$ and the perturbations vanish, we recover the integral constraint (13) on the net up-slope transport from the 1D solution, $\Psi_\infty/L_y = \kappa_{\mathrm{BG}} \cot\theta$.

Callies (2018) proposes a simple parameterization of restratification by 3D submesoscale baroclinic eddies as a way to account for these missing physics in the 1D boundary layer solution. The main effect of baroclinic eddies is to extract available potential energy from the mean flow by slumping sloping buoyancy surfaces back towards the horizontal, thereby maintaining a realistically-large near-bottom stratification; this adiabatic process is most conventionally parameterized as an eddy overturning circulation (Gent and McWilliams 1990; Fox-Kemper et al. 2008). Taking advantage of thermal wind balance ($fv_{\hat{z}} = b_{\hat{x}}$), the slumping of isopycnals by baroclinic instability—which decreases horizontal buoyancy gradients $b_{\hat{x}}$—can equivalently be parameterized as a reduction in the vertical shear $v_{\hat{z}}$, e.g. by enhanced vertical momentum diffusion (Rhines and Young 1982; Greatbatch and Lamb 1990; Young 2011). We provide a derivation of this closure in the Appendix, in which we apply Andrews and McIntyre's (1976) Transformed Eulerian Mean and Gent and McWilliams's (1990)'s baroclinic eddy parameterization scheme to the slope-aligned framework.

Following Callies (2018), we thus parameterize submesoscale eddy restratification by artificially increasing the vertical eddy viscosity $\nu = \sigma\kappa$. Unlike Callies (2018), who simply tune $\sigma = 230$ to match the mean behavior of their 3D model, however, we: 1) only enhance the viscosity $\nu_v = \sigma_v \kappa$ acting on the along-slope thermal wind (as in Holmes et al. 2019) since the available potential energy that fuels the instabilities is stored in cross-slope buoyancy gradients; 2) we allow the eddy viscosity to have vertical structure, $\sigma_v = \sigma_v(z)$, and 3) we estimate the magnitude and structure of $\sigma_v(z)$ from the eddy fluxes resolved by a 3D model (Figure 1b; see Appendix). We refer to $\Psi + \frac{\langle wb \rangle}{N^2 \sin\theta L_x}$ as the cross-slope *residual* transport (analogous to that of the Southern Ocean, e.g. Marshall and Radko 2003), since the eddy flux term is equal to the eddy overturning streamfunction in the limit of stationary and adiabatic eddies, which is applicable outside of the thin BBL (Figure 11c; see Appendix).

Applying this simple closure to the 1D model results in weakening of the slope-normal shear of the along-slope flow and, because of the approximate thermal wind balance $fv_z \simeq b_z \sin\theta$ that holds in the SML (eq. 8), results in a corresponding weakening of the negative perturbation stratification b_z (equivalent to a strengthening of the total stratification B_z; compare dash-dotted and solid lines in Figure 1a). In this context, the 1D model's up-slope transport ψ is re-interpreted as the residual transport, since it also includes the eddy-induced overturning. At equilibrium, this parameterized eddy restratification triples B_z and thus also

κB_z and the residual flow ψ at the top of the 1D solution's BBL (Figure 1a and Figure 8a,b), bringing the watermass transformations of the 1D BBL more in line with the basin-scale overturning (Morris et al. 2001; Callies 2018).

3. Numerical model setup

We simulate 3D mixing-driven flows using the hydrostatic Boussinesq equations in the MIT General Circulation Model (MITgcm; Marshall et al. 1997). For simplicity, we assume a linear equation of state; because temperature units are more intuitive, we use temperature T and buoyancy $b \equiv g\alpha T$ interchangeably throughout, where $g = 9.81\,\mathrm{m/s^2}$ is the gravitational acceleration and $\alpha = 2 \times 10^{-4}\,°\mathrm{C}^{-1}$ is a constant thermal expansion coefficient.

a. Realistic bathymetry

Most of the results describe a core realistic-bathymetry simulation of the Brazil Basin subregion sampled by both the Brazil Basin Tracer Release Experiment (BBTRE, Ledwell et al. 2000) and Dynamics of the Mid-Ocean Ridge Experiment (DoMORE, Clément et al. 2017), located on the western flank of the Mid-Atlantic Ridge. We extract the Brazil Basin's seafloor topography from the Global Bathymetry and Topography at 15 Arc Sec dataset (SRTM15+; Tozer et al. 2019), which includes many more multibeam measurements than previous products (e.g. Smith and Sandwell 1997) and thus better resolves both the BBTRE fracture zone canyon at 21°30' S and the smaller-scale abyssal hills characteristic of mid-ocean ridges (Figure 3a). We interpolate the bathymetry onto a locally tangent Cartesian grid $(\hat{x}, \hat{y}, \hat{z})$ aligned with the BBTRE canyon, where $\hat{x}$ denotes the along-canyon dimension and $\hat{y}$ denotes the cross-canyon dimension (Figure 3a), and produce a gridded bathymetry field $\hat{d}(\hat{x}, \hat{y})$. The simulated canyon stretches from a few km west of the Tracer Release

Experiment site around 18.5 °W (Ledwell et al. 2000) to a few km east of the DoMORE sill that dramatically constrains the up-canyon flow at 14.5 °W (Clément et al. 2017).

b. Implementing the perturbation Boussinesq equations in the mean-slope coordinate frame

Following Section 2a, we solve equations (1–5) in a coordinate frame aligned with the domain's mean slope. Equations (1–5) are solved in terms of the perturbation variables, with the background buoyancy field $N^2\hat{z}$ entering only indirectly via linear and inhomogeneous terms in the perturbation buoyancy equation, implemented as additional explicit tendency terms in the MITgcm. To stabilize the numerical solution without damping submesoscale eddies, we additionally implement horizontal (in the rotated frame) biharmonic hyper-diffusion of momentum and buoyancy which acts only at scales close to the grid resolution. Horizontal hyper-diffusive tendencies vanish in the budgets presented here, so we omit them in all of our analyses. We enforce an insulating boundary condition on the full buoyancy at the seafloor: $\mathbf{n} \cdot (\kappa \nabla B) = 0$.

Relative to the mean slope, the anomalous seafloor topography $d(x, y) \equiv \hat{d}(\hat{x}, \hat{y}) - \hat{x} \tan\theta$ is nearly continuous across the periodic boundaries in the along-canyon direction $\mathbf{x}$ and in the cross-canyon direction $\mathbf{y}$; however, to eliminate any remaining discontinuities across these boundaries, we join the two boundaries smoothly by linear interpolation in both $\mathbf{x}$ and $\mathbf{y}$.

By 1) removing the uniformly-stratified background state from the prognostic variables, 2) formulating the model in the slope coordinate frame, and 3) making the boundary conditions and forcing terms periodic in the (x, y) plane, we are free to apply periodic boundary conditions to the perturbation state variables u, v, b, and p in both $\mathbf{x}$ and $\mathbf{y}$.

c. *Forcing by observation-inspired bottom-enhanced turbulent mixing*

Following the classic one-dimensional boundary layer configuration (Wunsch 1970), we parameterize small-scale turbulent mixing as a slope-normal[5] diffusive buoyancy flux $-\kappa\, \partial_z B\, \mathbf{z}$. We use Callies' (2018) self-similar height-above-bottom profile

$$\kappa(x, y, z) = \kappa(z; d) = \kappa_{\text{BG}} + \kappa_{\text{BOT}} \exp\left(-\frac{z + d}{h}\right), \tag{17}$$

with $\kappa_{\text{BOT}} = 1.8 \times 10^{-3}\,\text{m}^2/\text{s}$, $\kappa_{\text{BG}} = 5.3 \times 10^{-5}\,\text{m}^2/\text{s}$, and $h = 230\,\text{m}$; these parameter values are chosen by performing a least-squares fit to the height-above-bottom-average of 126 microstructure profiles in the BBTRE region. The sparsity and noisiness of individual mixing profiles, and disagreements in the literature about where mixing in strongest (Polzin et al. 1997; St. Laurent et al. 2001; Polzin 2009; Clément et al. 2017; Thurnherr et al. 2020), prohibit the formulation of a robust parameterization with a richer spatial structure. We imagine this imposed bottom-enhanced mixing to represent a variety of turbulent ocean processes (see Thorpe 2005), especially the breaking of internal waves (Whalen et al. 2020) but also including unspecified boundary mixing processes (Armi 1978; Armi and D'Asaro 1980; Polzin et al. 2021).

d. *Numerics*

The horizontal grid spacing of $\Delta x = \Delta y = 600\,\text{m}$ is fine enough to permit the anticipated submesoscale baroclinic turbulence, which for the 1D sloping BBL problem has a maximum linear growth rate near the local deformation radius $L \sim \frac{NH_{\text{ML}}}{f} = 6\,\text{km}$ (Stone 1966; Wenegrat et al. 2018), where $H_{\text{ML}} \approx 250\,\text{m}$ is the thickness of the weakly-stratified bottom layer (Callies 2018). Yet, the grid spacing is also coarse enough for a three-dimensional

[5] Vertical buoyancy gradients are generally much larger than horizontal gradients, so, assuming an isotropic diffusivity, the vertical (or, for small slopes $\theta \ll 1$, approximately slope-normal) components of the diffusive buoyancy flux dominate.

simulation of the entire 480 km by 60 km region to be computationally feasible. We set the hyper-diffusivities $\kappa_4 \equiv \nu_4 = 2 \times 10^4\,\mathrm{m}^4/\mathrm{s}$, the smallest value that maintains a stable solution, so that hyper-diffusion interferes minimally with diapycnal buoyancy fluxes and the growth of submesoscale instabilities (Callies 2018; Ruan and Callies 2020). In the vertical, a cell thickness of $\Delta z = 6\,\mathrm{m}$ (with partial cells down to 1.2 m) marginally resolves the predicted $\mathcal{O}(10\,\mathrm{m})$-thick BBL. A high-resolution 1D spin-up experiment confirmed this vertical resolution is sufficient to accurately reproduce all features of the analytical solution (using Burns et al.'s 2016 Dedalus package; not shown). Starting at about 1000 m above the mean slope, the cell thickness Δz is increasingly stretched (up to $\Delta z = 50\,\mathrm{m}$ at the top of the domain) to efficiently fit both the $h \log(\kappa_{\mathrm{BOT}}/\kappa_{\mathrm{BG}}) \approx 1300\,\mathrm{m}$ vertical scale of abyssal mixing layers (Callies 2018) and the $\mathcal{O}(800\,\mathrm{m})$ topography into a domain that spans a height $H = 2700\,\mathrm{m}$ above the mean slope.

e. Parameter regime

Following Callies (2018), we assume a background far-field stratification $N = 1.3 \times 10^{-3}\,\mathrm{s}^{-1}$ and a local Coriolis parameter $f = -5.3 \times 10^{-5}\,\mathrm{s}^{-1}$ characteristic of the BBTRE region. Applying a linear fit to the bathymetry $\hat{d}(\hat{x}, \hat{y})$ yields the domain's average topographic slope angle $\theta = 1.26 \times 10^{-3}$ in $\hat{\mathbf{x}}$. We assume that small-scale turbulent mixing acts similarly to mix buoyancy and momentum, i.e. we assume a turbulent Prandtl number of $\sigma \equiv \frac{\nu}{\kappa} = 1$. Because we resolve submesoscale instabilities, we do not need to parameterize their restratification by increasing σ. Mixing layers are thus characterized by weak stratification and gentle large-scale slopes, equating to a small slope Burger number, $S \equiv N^2 \tan^2\theta / f^2 = 10^{-3} \ll 1$ and BBL thickness $\delta \approx 8\,\mathrm{m}$ (eq. 11).

We spin up the simulations from a uniformly-stratified rest state ($b = 0, p = 0, \mathbf{u} = \mathbf{0}$). The BBL adjusts rapidly on a timescale $\tau_{\text{BBL}} = \delta^2/\kappa_{\text{BOT}} = 10\,\text{hours}$. While the full equilibration of the solution occurs over a prohibitively long diffusive timescale characteristic of the abyssal ocean interior, $\tau_{\text{INT}} = H^2/\kappa_{\text{BG}} \approx 5000\,\text{years}$, buoyancy tendencies are small enough by $t = 13\,\text{years}$ in the bottom 1000 m (see Section 5) that we consider the solution sufficiently equilibrated for the analyses presented here.

f. Hierarchy of progressively idealized simulations

The simulations in our model hierarchy differ only in their seafloor topography, domain length, and dimensionality. We progressively idealize the BBTRE canyon configuration (Figure 3f): first, we remove the abyssal hills along the ridge flank and idealize the geometry of the remaining canyon and sill features ("Canyon+Sill"; Figure 3e); second, we remove the sill ("Canyon"; 3d); third, we remove the canyon entirely ("Smooth3D"; Figure 3c); and finally, we eliminate variations along the plane of the slope, collapsing the solution onto a single slope-normal dimension as in classical BBL theory ("1D"). For reference, we also include some additional variants on the 1D model where we vary one parameter at a time: non-rotating ("$1\text{D}_{f=0}$"), non-sloping ("$1\text{D}_{\theta=0}$"), and parameterized submesoscale eddies ("$1\text{D}_{\sigma_v(z)}$"; see Appendix). Unless we specify otherwise, results refer to the realistic-topography BBTRE simulation.

4. Mixing-driven up-canyon flow, submesoscale turbulence, and stratification

At quasi-equilibrium, the time-mean flow (averaged over days 5000 to 5500) is dominated by a vigorous up-canyon jet along the canyon thalweg, banked along the steeper southern flank of the canyon (as in Dell 2013; Ruan and Callies 2020). The up-canyon jet exhibits a maximum along-canyon-averaged velocity of $\overline{u}^x = 0.75\,\mathrm{cm/s}$ about 400 m above the seafloor (Figure 4a). This up-slope jet is non-uniform and partially compensated by a down-slope jet on the gentler northern flank, such that the maximum cross-canyon-averaged up-canyon velocity is reduced to $\overline{u}^y = \mathcal{O}(0.1\,\mathrm{cm/s})$ (Figure 4a,b). The up-slope jet accelerates as it spills over two major cross-canyon sills: the BBTRE sill at $x = 110\,\mathrm{km}$ and the DoMORE sill at $x = 420\,\mathrm{km}$ (Figure 4a,b); this acceleration and the spilling over of isopycnals at both sills is suggestive of hydraulic control[6] (Pratt and Whitehead 2008). The vertically-integrated cross-slope transport $\int_{z=0}^{H} u\,\mathrm{d}z$ is dominated by standing eddy features above the canyon (Figure 4c, recall $z = 0$ at the deepest point relative to the mean slope), but prominently features meandering up- and down-canyon jets when integration is restricted to just the canyon itself, $\int_{z=0}^{800\,\mathrm{m}} u\,\mathrm{d}z$ (Figure 4d). These simulated mixing-driven means flows can be compared against two in-situ mooring observations: the BBTRE mooring at $x = 110\,\mathrm{km}$, several km upstream of the BBTRE sill (Toole 2007; also analyzed by Thurnherr et al. 2005), and a DoMORE mooring at $x = 420\,\mathrm{km}$, atop the DoMORE sill (Clément et al. 2017). At the DoMORE sill, horizontal and vertical constrictions accelerate the simulated up-canyon flow to $5\,\mathrm{cm/s}$ over a layer $\delta z = 150\,\mathrm{m}$ thick and $\delta x = 2.5\,\mathrm{km}$ wide (Figure 5a). The resulting velocities are roughly constant in time, also suggestive of hydraulic control (Pratt and Whitehead 2008), and are about 25% those measured by the mooring (half as fast and half as thick; Figure 5b). By contrast, the simulated up-canyon flow at the BBTRE mooring is much weaker ($u \approx 0.75\,\mathrm{cm/s}$) but spread over a thicker ($\delta z \approx 600\,\mathrm{m}$) and wider ($\delta x \approx 5\,\mathrm{km}$) layer, such that the total up-canyon transports at the two sections are similar (Figure 5c). It is impossible to compare against observed *transports* because single mooring velocity profiles (e.g. Thurnherr et al. 2005) cannot be reliably extrapolated across the

[6] The DoMORE control section is evident from the canyon hydrography, but the BBTRE one is not (Thurnherr et al. 2005).

canyon, although such errors may be smaller at constrictions considerably narrower than the local deformation radius (Thurnherr 2000), as at the DoMORE sill. The simulated flow at the BBTRE mooring has roughly the same vertical structure as in the moored current meter velocities, but about half their magnitude (Figure 5d). The relative weakness of the simulated flows suggest that either the imposed microstructure-based mixing rates are biased low (as suggested by Thurnherr et al. 2005 and Clément et al. 2017, and by the in prep. tracer analysis by Ledwell and modelling by Odgen et al.) or that the simulation fails to capture important physics.

Averaging the BBTRE simulation in height-above-bottom (hab) coordinates reveals that the stratification generally remains close to its background value, except in the $\mathcal{O}(10\,\mathrm{m})$-thick BBL (Figure 6a, solid blue line). Upon first inspection, this result appears inconsistent with observations in the canyon which, when averaged in hab, exhibit much weaker stratification up to 600 m above the seafloor (Figure 6, dashed and dotted red lines). Most of this discrepancy is resolved by sampling the simulation at the exact locations of the observational profiles (Figure 6b), and comparing their sample mean to that of the observations (Figure 6a, red lines). Since the BBTRE sampling strategy was to find as much tracer as possible, the field campaign specifically focused on sampling the deep depressions in the BBTRE canyon, which appear to exhibit unusually weak stratification compared to the canyon flanks, sills, and the surrounding ridge flanks. However, several microstructure profiles from the 1996 cruise are available along the canyon crests—just north of the domain—and on average exhibit similarly strong near-bottom stratification as in the simulation's domain average (Figure 6a, dashed blue line). This conditional averaging exercise clarifies the significant disagreements in reported estimates of the BBTRE region's average stratification (Polzin et al. 1997; St. Laurent et al. 2001; Polzin 2009). But even accounting for sampling bias, the simulated canyon is more stratified by about a factor of two relative to the observations (see Section 6).

The time-mean view of the up-canyon circulation above filters out a rich field of submesoscale eddies which have radii comparable to the deformation radius and are trapped within a few hundred meters of the seafloor, including within the $\mathcal{O}(10\,\mathrm{km})$-wide canyon (Figure 7). These eddies manifest themselves as spatial and temporal meanders of the mean up-canyon jet, which in the following section we show contribute significantly to the simulation's buoyancy budget and to maintaining its strong near-bottom stratification.

5. Buoyancy budgets: mixing, mean flow, and eddies

In this section, we use a hierarchy of models to elucidate the complicated dynamics that support the up-canyon mean flows described in the previous section. Volume-integrated buoyancy budgets (eq. 16) provide the major insights and are presented in Figure 8 for each model in the hierarchy. We further separate the contributions from time-independent standing eddies and transient eddies. All of the solutions exhibit substantial residual tendencies several hundred meters above the topography; however, within a few hundred meters of the ridge flanks and within the canyons, tendencies are an order of magnitude smaller than other terms in the budgets because the dynamics (vigorous mixing and submesoscale processes) within the bottom few hundred meters are much faster than the weak diffusion in the interior (Figure 8, black). The 1D and $1\mathrm{D}_{\sigma_v(z)}$ simulations are computationally inexpensive, so we also provide their fully equilibrated solutions for context (Figure 8a,b; dotted).

In the classical 1D solution, a weak up-slope transport in the BBL (Figure 8a, blue line) maintains a weak near-boundary stratification, although it is already much stronger than in the flat-bottom after 5000 days of spin-up (Figure 9a). The evolution of the Smooth3D solution follows the 1D solution closely until about 800 days, at which point the laminar solution becomes unstable to submesoscale baroclinic modes which rapidly grow and equilibrate at finite amplitude (Callies 2018; Wenegrat et al. 2018). At quasi-equilibrium, these transient eddies advect denser waters from the SML back into the BBL (Figure 8b, orange), effectively restratifying the BBL (Figure 9b) and thus strengthening the maximum diffusive buoyancy flux (Figure 8b, red). It is helpful to interpret the combination of the mean flow and the eddy fluxes as the residual circulation that advects tracers (Ferrari and Plumb 2003; see Appendix). In this framing, the slope-normal eddy flux nearly doubles the residual upwelling in the BBL (Figure 8b,a, green lines). The crude eddy parameterization in $1\mathrm{D}_{\sigma_v(z)}$ qualitatively captures this restratifying effect (Figure 9b, compare dash-dotted and blue against solid grey) and enhances the residual BBL upwelling by a factor of 2–3 relative to the 1D model, both transiently and at equilibrium (Figure 8b,c; solid and dotted green lines, respectively). A more rigorous approach to parameterization is beyond the scope of this paper.

The volume-integrated buoyancy budget is more complicated to interpret in the presence of variable topography. In the Canyon solution, a substantial diffusive buoyancy flux convergence drives a vigorous up-slope mean flow within the bottom 200 m along the narrow trough of the canyon, producing a transport of 5 mSv (Figure 8d, blue) which is already larger than the total BBL transport in the 1D model (Figure 8a, blue). This strong mean flow maintains a stratification near the large background value within the canyon trough (Figures 10b; 9c, orange line). Thurnherr and Speer (2003) hypothesizes this efficient restratification is due to the canyon sidewalls blocking the along-slope thermal wind, such that the momentum is redirected into the cross-slope flow. The Canyon simulation's excellent agreement with the $1\mathrm{D}_{f=0}$ model, in which rotation is turned off and thus the along-slope thermal wind is suppressed by construction, supports their hypothesis (Figure 9c; orange and dotted lines). Ruan and Callies (2020) hypothesize that flow across the steep canyon flanks with $S = \mathcal{O}(1)$ also contributes significantly to the strong stratification in the canyon. However, this hypothesis does not explain the strong stratification along the canyon thalweg, where the cross-canyon slope goes to zero and local dynamics cannot sustain a finite stratification at equilibrium in the absence of an along-canyon topographic slope.

The turbulent buoyancy flux also converges around a Height Above the Mean Slope (HAMS) of $z = 800\,\mathrm{m}$, driving an additional residual upwelling of about $13\,\mathrm{mSv}$ from $z = 600\,\mathrm{m}$ to $800\,\mathrm{m}$ dominated by the BBLs on the upper canyon flanks and on the smooth ridge flank surrounding the canyon (Figure 8d, green line). The upwelling along the smooth ridge flank of the Canyon simulation is about twice as large as that of the Smooth3D simulation, despite covering a smaller area, because along-slope buoyancy gradients above the canyon flanks provide an additional energy source for submesoscale instabilities (Figure 10d), driving an isopycnal thickness flux between the canyon and surrounding flanks and thus maintaining a much larger stratification on the flanks (Figures 9b). In the Canyon simulation's quasi-equilibrium state, much of the turbulent buoyancy flux divergence in the upper SML (far above the seafloor) is not yet equilibrated: the bottom-enhanced diffusion of buoyancy towards the boundary slowly cools the interior (Figure 8d, red and black lines; MacCready and Rhines (1991)).

In the Canyon+Sill simulation, the sill blocks up-slope flow within the trough of the canyon (Figure 8e, d). This is expected, since the up-canyon flows of $\mathcal{O}(1\,\mathrm{cm/s})$ only carry sufficient kinetic energy to lift a parcel across a stratification of $N \sim \mathcal{O}(10^{-4} - 10^{-3}\,\mathrm{s}^{-1})$ by a height $\delta_{\mathrm{Fr}} = U/N \sim 20 - 200\,\mathrm{m}$ (based on a topographic Froude number of $\mathrm{Fr} \equiv N\delta_{\mathrm{Fr}}/U \sim 2$), much smaller than the sill height of $h_{\mathrm{sill}} = 800\,\mathrm{m}$ and resulting in a blocked flow layer of thickness $h_{\mathrm{sill}} - \delta_{\mathrm{Fr}}$ (Baines 1979; Winters and Armi 2012), both up- and down-stream of the sill (recall the cross-slope periodicity). No up-slope mean flow is available to restratify the trough of the canyon, so it slowly homogenizes due to mixing (Figure 10c; as in Dell 2013). In contrast, within a slope-normal displacement δ_{Fr} of the sill, mean flows along the upper parts of the two canyon flanks are able to maintain a layer of strong stratification[7] (Figures 8e, 10e,f).

The structure of the stratification in the BBTRE simulation is qualitatively similar to that of the Canyon+Sill simulation, although the rougher abyssal hill topography acts to thicken the layer of enhanced stratification near the DoMORE sill height and supports a large near-bottom stratification on the hilly ridge flanks surrounding the canyon (Figure 10g,h, 9b). The slope-normal structure of the BBTRE canyon's buoyancy budgets (Figure 8f) is remarkably similar to that of the Canyon+Sill simulation and can thus be explained as the combination of the processes described—only sightly blurred in the slope-normal direction by the additional topographic roughness.

6. Conclusions and Discussion

By generalizing the methods of classical 1D sloping Bottom Boundary Layer (BBL) theory (Garrett et al. 1993), we construct a hierarchy of mixing-driven flow simulations that bridge the gap between three-dimensional (Armi 1978) and one-dimensional (Garrett 1979) conceptual models of abyssal mixing layer restratification. Our choice to parameterize small-scale turbulence as a bottom-enhanced turbulent diffusivity—inspired by local microstructure measurements—considerably simplifies the analysis but may not adequately represent the

[7]Tidal velocities, omitted for simplicity here, would imply a larger excursion height, a thinner blocked flow layer, and the potential for restratification processes to penetrate deeper into the canyon trough (as hypothesized by Clément et al. 2017).

underlying small-scale physics (see Polzin and McDougall 2022). Nevertheless, in this conventional prescribed-diffusivity framework we demonstrate that the homogenizing tendency due to bottom-enhanced small-scale mixing is balanced by the restratifying effects of the residual overturning circulation, which is a combination of mean and submesoscale eddy flows (eq. 16). At equilibrium, the slow interior diffusion of heat into the abyss is balanced by a weak net upwelling (eq. 13), the result of substantial cancellation of up- and down-slope flows.

The simulations' steady states are never achieved here due to the prohibitively slow diffusive adjustment in the interior (MacCready and Rhines 1991); in more realistic contexts, cross-slope pressure gradients due to coupling with the non-local circulation would support a much more rapid adjustment process (Peterson and Callies 2021). Despite the non-equilibrated nature of our solutions, the slope-aligned framework permits simplified buoyancy budgets which facilitate our dynamical interpretation and the derivation of an eddy closure (see Appendix). Another advantage of the slope-aligned framework is that the solutions are less ambiguous than previous approaches, which either require ad hoc sponge layers at distant horizontal boundaries (Dell 2013) or can only be analyzed transiently before mixing completely homogenizes buoyancy (Ruan and Callies 2020). The slope-aligned framework also permits a consistent exploration of ever more realistic configurations: from a constant topographic slope—well described by 1D BBL models (Garrett et al. 1993)—to the complex geometry of the region surrounding the BBTRE canyon. While the local nature of the sloping BBL framework is conceptually convenient for all of the above reasons, several important non-local factors have been ignored. For example, the inclusion of cross-slope pressure gradients (Peterson and Callies 2021) or large-scale boundary currents (MacCready and Rhines 1991; Naveira Garabato et al. 2019) would fundamentally alter the transient spin-up problem. The periodic nature of the simulation may also overemphasize topographic blocking effects since upstream topographic sills also re-appear downstream.

The results of our quasi-realistic simulation of the Brazil Basin Tracer Release Experiment (BBTRE) reconciles two dominant boundary mixing paradigms: yes, bottom-enhanced mixing drives a restratifying up-slope flow in the BBL (Garrett 1979, 1990); but, this flow is much stronger than predicted by 1D theory due to net restratification by transient baroclinic eddies and topographic steering/blocking (Armi 1978, 1979a; Thurnherr and Speer 2003; Callies 2018; Ruan and Callies 2020). The net restratifying effect can to a large extent be attributed to three distinct physical restratification/destratification processes:

1. slumping of isopycnals by finite-amplitude submesoscale baroclinic instabilities (Wenegrat et al. 2018; Callies 2018),
2. the blocking of cross-canyon thermal winds within narrow fracture zone canyons (Thurnherr and Speer 2003; Dell 2013; Ruan and Callies 2020), and
3. the effect of sills in blocking up-canyon mean flows and homogenizing depressions well below the sill height (Baines 1979; Winters and Armi 2012; Dell 2013).

We propose a simple parameterization for the restratifying effects of submesoscale baroclinic eddies in terms of a vertically-varying enhancement of vertical momentum diffusion (see Appendix). The blocking of along-slope flow by canyon walls can be captured in the 1D model by inhibiting the development of along-slope thermal wind, such as by setting $f = 0$.

Applied to the BBTRE model, the slope-averaged buoyancy budget (16) confirms Thurnherr et al.'s (2020) hypothesis that spatial averaging reconciles the thin *local* BBL transformations implied by vertical microstructure profiles and 1D models (e.g. Thompson and Johnson 1996) with the thicker *bulk* BBL transformations implied by a decreasing topographic perimeter—or mixing area—with depth (Polzin 2009; Kunze et al. 2012; Holmes et al. 2018): water below the canyon crest upwells in the net, while water above downwells (Figure 16f). The spatial heterogeneity of the simulated up-canyon flow (Figures 5,6) may explain why the buoyancy fluxes estimated from microstructure profiles are much too weak to balance the upwelling transports inferred by uniformly-extrapolated moored velocity estimates (Thurnherr et al. 2005).

Our quasi-realistic simulations provide the first BBL- and submesoscale-resolving simulations of the mixing-driven abyssal overturning in the Brazil Basin, complementing Huang and Jin (2002) and Ogden and Ferrari's (in prep) coarser-resolution basin-scale simulations. Despite the idealization of our numerical set-up, we qualitatively reproduce key features of the observations: broad up-slope flow and near-boundary stratification of $B_z \approx \mathcal{O}(10^{-7}\mathrm{s}^{-2})$ along the canyon trough (Toole 2007; Ledwell et al. 2000), stronger near-bottom stratification along the hills surrounding the canyon (Polzin 2009), hydraulically accelerated flow over blocking sills (Clément et al. 2017), and the mean diapycnal downwelling and spreading of a tracer released in the SML (Ledwell et al. 2000; see submitted companion manuscript, Drake et al. 2022). Despite this qualitative agreement, the simulated diapycnal transports within the canyon are too weak—and the stratification too strong—by roughly a factor of 2. These remaining discrepancies could be explained by the previously mentioned limitations of the inherently local slope-aligned modelling framework and the self-similar parameterization of small-scale mixing. The lack of full equilibration of the simulations could explain the too-strong stratification—the 1D models become about half as stratified at equilibrium—but not the too-weak up-canyon flow. Too-weak canyon mixing, on the other hand, could potentially explain both biases: we speculate that microstructure-based estimates of the turbulent diffusivity may be biased low due to sampling biases (Watson et al. 1988; Voet et al. 2015; Cael and Mashayek 2021; Whalen 2021) or biases in the mixing parameterization (Ijichi et al. 2020). Based on observations and basin-scale simulations of tracer spreading, respectively, Ledwell (in prep) and Ogden and Ferrari (in prep) similarly conclude that tracer observations are more consistent with diffusivities about 2 times larger than those inferred from microstructure[8].

The characteristic topographic features in the BBTRE (large-scale slope, canyon, and hills) are typical of mid-ocean ridges, such that the dynamics described here can be thought to apply to the global mid-ocean ridge system (with the steepness of slopes and hills modulated by the age of the rift valley and the Coriolis parameter by its latitude). The BBTRE simulation exhibits an instantaneous diapycnal upwelling transport in the BBL of $\mathcal{E}_{\text{BBL}} = 60\,\text{mSv}$, where $\mathcal{E} = \frac{1}{\Delta b}\int_{\mathcal{V}(|b-b'|<\Delta b/2)} \nabla \cdot (\kappa \nabla b')\mathrm{d}V$ is the average watermass transformation rate within a volume $\mathcal{V}$ for a layer of thickness Δb and $\mathcal{E}_{\text{BBL}}$ confines this integral strictly to regions of buoyancy flux convergence (see submitted companion manuscript, Drake et al. 2022). The upwelling transport suggested by the bulk buoyancy budget presented here (Figure 8f) is smaller than $\mathcal{E}_{\text{BBL}}$ by a factor of three due to substantial cancellation from temporal averaging and opposing cross-slope flows at the same height above the mean slope (e.g. Figure 4a). Extrapolating these BBL watermass transformations to the length of the Mid-Atlantic Ridge in the Brazil Basin (about 55 times the domain width $L_y = 60\,\text{km}$), this 3.3 Sv of BBL upwelling[9] would alone balance much of the 3.7–4.0 Sv net inflow of Antarctic Bottom Water in the Brazil Basin (Hogg et al. 1982; Morris et al. 2001). Extrapolating even

[8] Given the uncertainties of the microstructure methods, agreement within a factor of 2 is generally considered to be good (e.g. Gregg et al. 2018).

[9] This is much larger than Ruan and Callies' (2020) estimate of 0.5 Sv because our near-bottom stratification on the ridge flanks is much stronger than theirs, due to a combination of restratification effect of abyssal hills and fundamental differences between the slope-aligned and transient model configurations (see Peterson and Callies 2021).

further to a global mid-ocean ridge system of length 80×10^3 km (including both flanks of the ridge; Thurnherr et al. 2005) leads to a global BBL upwelling of 80 Sv due to upwelling along mid-ocean ridges, roughly consistent with global diagnostic estimates of BBL upwelling (Ferrari et al. 2016; McDougall and Ferrari 2017).

Global extrapolations of localized estimates of BBL upwelling, such as the above, have been used to attribute the *net* abyssal overturning to individual mixing hotspots (e.g. Ferron et al. 1998; Voet et al. 2015; Thurnherr et al. 2020; Spingys et al. 2021). These observations, however, generally also imply significant downwelling in adjacent buoyancy classes, suggesting that their localized upwelling may be offset by a similar dynamical process operating nearby—but centered on a different buoyancy surface. For example, Thurnherr et al. (2020) argue that the observed turbulent buoyancy flux convergence in the BBTRE canyon, extrapolated to all of the fracture zone canyons in the Brazil Basin, is sufficient to transform "the total inflow of AABW". Above the canyon, however, their own observations imply an opposing buoyancy flux divergence of comparable magnitude; upwelling within the canyon is thus only half of the story. Consider the following heuristic argument which applies the slope-aligned buoyancy budgets derived in Section 2c in buoyancy coordinates. Following the $\gamma_n \in \{28.1, 28.15\}\,\mathrm{kg/m^3}$ neutral density class in Thurnherr et al.'s (2020) Figure 3, for example, we apply eq. (16) to their integrated buoyancy fluxes in Figure 7 to infer a bulk upwelling of $\Psi(z_{\text{crest}}) \simeq \frac{\langle wb \rangle / L_x}{N^2 \sin\theta} \simeq \frac{\Gamma \int \epsilon \, \mathrm{d}y}{N^2 \sin\theta} \approx \frac{0.2\left(2 \times 10^{-5}\,\mathrm{m^3/s^3}\right)}{\left(1 \times 10^{-6}\,\mathrm{s^{-2}}\right)\left(2 \times 10^{-3}\right)} = 10\,\mathrm{mSv}$ within the canyon at the DoMORE site[10]. This confirms Thurnherr et al.'s (2020) central conclusion that—regardless of the shape of individual buoyancy flux profiles—the concave canyon topography implies that the *integrated* flux peaks at the crest of the canyon and thus drives a substantial bulk upwelling within the canyon. A few hundred km down-canyon, however, this same

[10]Averaging the overflow and non-overflow profiles, for simplicity.

density class rests above the canyon and experiences a net buoyancy flux divergence, driving a downwelling of $\Psi(z_{\text{crest}} + 500\,\text{m}) - \Psi(z_{\text{crest}}) \approx -4\,\text{mSv}$ that partially compensates for the upwelling in the canyon and suggests a significantly weaker *net* upwelling of 6 mSv for the BBTRE canyon. This heuristic exercise serves as a cautionary tale for attributing abyssal upwelling to individual regions or processes: both strictly positive and strictly negative components of watermass transformations along a buoyancy surface must be accounted for to robustly characterize the net overturning circulation.

At a global scale, diagnostic estimates of watermass transformations suggest significant compensation is the norm, exhibiting typical amplification factors of $\mathcal{A} \equiv \mathcal{E}_{\text{BBL}}/\mathcal{E}$ of 2 to 5, where $\mathcal{E} = \mathcal{E}_{\text{BBL}} + \mathcal{E}_{\text{SML}}$ is the net diapyncal transport and $\mathcal{E}_{\text{SML}}$ is the downwelling in the stratified mixing layer (Ferrari et al. 2016; McDougall and Ferrari 2017; Cimoli et al. 2019). However, these diagnostic exercises do not provide any insight into the physics underlying the observed density structure that supports these transformations. More problematically, these results seem to contradict the weak upwelling with $\mathcal{A} \simeq 1$ implied by 1D boundary layer dynamics (Section 2b). Building upon Callies (2018) and Ruan and Callies (2020), our prognostic modelling approach demonstrates how three-dimensional eddy and topographic effects conspire to provide sufficient restratification to support a significant upwelling/downwelling dipole, i.e. $\mathcal{A} \gg 1$ (Figure 8a,f). Our results inspire two open questions: 1) which topographic regimes (e.g. ridges, slopes, plains) or topographic roughness features (e.g. hills, canyons, channels, sills, or seamounts) contribute the most to abyssal watermass transformations (e.g. Armi and D'Asaro 1980; Bryden and Nurser 2003; Thurnherr et al. 2005; Legg et al. 2009; Nazarian et al. 2021; Mashayek et al. 2021) and 2) what are the dynamics that support finite watermass transformations in these regions (Garrett 1979, 1990; Callies 2018; Drake et al. 2020)?

Our combined assumptions of constant background stratification and zero barotropic cross-slope pressure gradient assert that the net upwelling scales with the background diffusivity (eq. 13) and thus that the net upwelling $\Psi_\infty = \mathcal{E}$ is very small. While our local model helps explain the magnitude of bottom boundary layer upwelling $\mathcal{E}_{\text{BBL}}$, it does not meaningfully constrain $\mathcal{E}_{\text{SML}}$ or $\mathcal{A}$. Salmun et al. (1991) use asymptotic analysis to show that small perturbations away from a constant interior stratification drive an exchange flow between the boundary and the interior, which then feeds back on the interior stratification. In the context of the abyssal ocean, vertical variations in the basin-scale interior stratification are relatively large, such that they enter as leading-order terms in watermass transformations (Spingys et al. 2021) and drive substantial exchange between the mixing layers and the interior (Holmes et al. 2018). In Drake et al.'s (2020) idealized basin-scale simulations, this boundary–interior coupling results in a substantial reduction of $\mathcal{E}_{\text{SML}}$, permitting an amplification factor of $\mathcal{A} = 1.5$ much smaller than the $\mathcal{A} \gg 1$ governed by local dynamics. These idealized prognostic model results are qualitatively consistent with the diagnostic approaches described above, but quantitative understanding of $\mathcal{E}_{\text{BBL}}$, $\mathcal{E}_{\text{SML}}$, and $\mathcal{A}$ remains incomplete.

Understanding of bottom-enhanced mixing has advanced considerably in recent years due to a combination of breakthroughs in observation (e.g. Polzin et al. 1997; Ledwell et al. 2000), theory (e.g. Polzin 2009), and modelling (e.g. Nikurashin and Legg 2011). The interpretation of these results in terms of broad diapycnal downwelling in the SML atop vigorous diapycnal upwelling in a BBL (Ferrari et al. 2016), however, is challenged by higher-resolution observations (van Haren 2018; Naveira Garabato et al. 2019; Polzin et al. 2021) and simulations (Gayen and Sarkar 2011; Kaiser 2020) of mixing processes within the bottom few dozen meters of the ocean. In addition to the debate on the nature of boundary mixing itself (see Polzin and McDougall 2022), the role of the resulting boundary layer flows in the global overturning circulation remains shrouded by poor understanding of their coupling to the far-field interior (Drake et al. 2020; Peterson and Callies 2021).

Acknowledgments. We thank the crews of the BBTRE and DoMORE field campaigns for collecting the observations that motivated this work. We acknowledge funding support from National Science Foundation Awards 6932401 and 6936732. This material is based upon work supported by the National Science Foundation Graduate Research Fellowship Program under Grant No. 174530. Any opinions, findings, and conclusions or recommendations expressed in this material are those of the author(s) and do not necessarily reflect the views of the National Science Foundation. This research is also supported by the NOAA Climate and Global Change Postdoctoral Fellowship Program, administered by UCAR's Cooperative Programs for the Advancement of Earth System Science (CPAESS) under award #NA18NWS4620043B.

Data availability statement. The source code for the MITgcm simulations and all of the Python code necessary to produce the figures will be publicly available at `github.com/hdrake/sim-bbtre` upon acceptance (or earlier by requesting the corresponding author). Our analysis of labeled data arrays is greatly simplified by the `xarray` package in Python (Hoyer and Hamman 2017).

APPENDIX

One-dimensional model of restratification by submesoscale baroclinic eddies along a sloping boundary

Our goal is to reformulate the 1D sloping BBL model using Transformed Eulerian Mean (TEM) theory (Andrews and McIntyre 1976) to facilitate the inclusion of submesoscale eddy restratification. We begin by assuming there are no large-scale variations in the perturbations, so that we can average in the along-slope (y) and cross-slope (x) directions and drop cross- and along-slope gradients. Then, averaging the slope-aligned equations (1–5) in both x and y, we have

$$\overline{u}_t - f\overline{v}\cos\theta - \overline{b}\sin\theta - \partial_z\left(\kappa\overline{u}_z\right) = -\partial_z\left(\overline{w'u'}\right), \tag{A1}$$

$$\overline{v}_t + f\overline{u}\cos\theta - \partial_z\left(\kappa\overline{v}_z\right) = -\partial_z\left(\overline{w'v'}\right), \tag{A2}$$

$$\overline{p}_z - \overline{b}\cos\theta = 0, \tag{A3}$$

$$\overline{b}_t + \overline{u}\,N^2\sin\theta - \partial_z\left(\kappa\overline{B}_z\right) = -\partial_z\left(\overline{w'b'}\right), \tag{A4}$$

where the eddy fluctuations $\phi' \equiv \phi - \overline{\phi}$ are departures from the slope–average means $\overline{\phi}$, $\overline{w} = 0$ from continuity and the no-flux bottom boundary condition, and we assume $\sigma = 1$.

We introduce the residual velocities

$$\left(u^\dagger, w^\dagger\right) \equiv \left(\overline{u}, \overline{w}\right) + \left(-\partial_z, \partial_x\right)\psi_e, \tag{A5}$$

which add to the Eulerian mean flow $\overline{\mathbf{u}}$ an eddy-induced overturning $\nabla \times \mathbf{y}\psi_e$ in the (x, z) plane that is by definition also non-divergent.

Using a convenient definition of the eddy streamfunction—Plumb and Ferrari (2005) show that its definition is not unique—inspired by Andrews and McIntyre (1976) but in a rotated coordinate frame,

$$\psi_e \equiv \frac{\overline{u'b'}}{\overline{B}_z}, \tag{A6}$$

we express the slope-averaged equations (A1—A4) in terms of the residual circulation $\mathbf{u}^\dagger = (u^\dagger, \overline{v}, w^\dagger)$. Since, by assumption, the large-scale average solution is independent of x, we have $\partial_x \psi_e = 0$ and thus $w^\dagger = \overline{w} = 0$. With this choice of eddy streamfunction (A6) and associated residual velocity, the momentum and buoyancy budget take the form,

$$\overline{v}_t + f u^\dagger \cos\theta - \partial_z \left(\kappa \overline{v}_z\right) = -\partial_z \left(\overline{w'v'} + f \cos\theta \, \frac{\overline{u'b'}}{\overline{B}_z} \right), \tag{A7}$$

$$\overline{b}_t + u^\dagger N^2 \sin\theta - \partial_z \left(\kappa \overline{B}_z\right) = -\partial_z \left[\frac{\overline{\mathbf{u}'b'} \cdot \nabla \overline{B}}{\overline{B}_z} \right], \tag{A8}$$

where we recall the total buoyancy is decomposed as $B \equiv N^2 \hat{z} + \overline{b} + b'$. The main advantage of working in terms of residual velocity is that only the eddy flux terms normal to density surfaces appears in the buoyancy budget. The mean slope of isopycnals in the rotated reference frame is given by $-\overline{B}_x/\overline{B}_z = -N^2 \sin\theta/(N^2 \cos\theta + \overline{b}_z)$ because $\overline{b}$ is independent of x. Thus $\overline{\mathbf{u}'b'} \cdot \nabla \overline{B}$ is the dot product of the eddy buoyancy flux with the mean buoyancy gradient, which is punishingly small because the submesoscale eddies are characterized by large Richardson numbers and do not generate mixing across density surfaces, as illustrated in Figure 11b for our numerical solutions. Then, at leading order,

$$\overline{b}_t + u^\dagger N^2 \sin\theta - \partial_z \left(\kappa \overline{B}_z\right) = 0, \tag{A9}$$

and the eddy closure problem is confined to the residual along-slope momentum flux (A7). This is the main advantage of working in terms of residual velocity, $\mathbf{u}^\dagger$, instead of Eulerian mean velocity. The residual velocity is the mean Lagrangian velocity that advects tracers, without additional contributions from eddy fluxes as can be seen in equation (A9).

Assuming quasi-geostrophic scaling for the eddy fluxes, the Reynolds flux term in (A7) is $\mathcal{O}(R_o)$ smaller than the buoyancy flux term and can be neglected. Closing the system then only requires a closure for the cross-slope eddy buoyancy flux $\overline{u'b'}$ that appears in the y-momentum equation. Following the argument proposed by Gent and McWilliams (1990); Gent et al. (1995), i.e. that quasi-geostrophic eddies generated through baroclinic instability act to fallten isopycnals and thus release available potential energy, we assume that the truly horizontal buoyancy flux is down-gradient,

$$\overline{\hat{u}'b'} \simeq -K(z)\overline{B}_{\hat{x}}. \tag{A10}$$

This closure can be expressed in slope coordinates, $\overline{B}_{\hat{x}} = -\bar{b}_z \sin\theta$, such that

$$K(z) = -\frac{\overline{\hat{u}'b'}}{\overline{B}_{\hat{x}}} = -\frac{\overline{u'b'}\cos\theta - \overline{w'b'}\sin\theta}{-\bar{b}_z \sin\theta} = \frac{\overline{u'b'}}{\overline{B}_z}\,\frac{N^2 + \bar{b}_z\cos\theta}{\bar{b}_z \sin\theta}, \tag{A11}$$

where we used the fact that the flux normal to density surfaces vanish and thus $\overline{w'b'} = -\overline{u'b'}\,\overline{B}_x/\overline{B}_z$. It is worth noting that $\overline{B_{\hat{z}}} = N^2 + \bar{b}_z\cos\theta$ is the true-vertical buoyancy gradient.

To clarify the role of this additional eddy-induced overturning, we focus on the stratified interior above the frictional bottom layer, where geostrophic balance applies to the mean along-slope flow in the mean cross-slope ($\mathbf{x}$) momentum equation (as in semi-geostrophic theories of frontogenesis),

$$-f\overline{v}_z \cos\theta = \bar{b}_z \sin\theta. \tag{A12}$$

Combining (A11) and (A12) and plugging back into (A7) yields

$$\overline{v}_t + f u^\dagger \cos\theta = \partial_z\left(\nu_e(z)\overline{v}_z\right), \tag{A13}$$

where we defined

$$\nu_e(z) \equiv \sigma_v(z)\kappa(z) \qquad \text{with} \qquad \sigma_v(z) \equiv 1 + \frac{K(z)}{\kappa(z)}\,\frac{f^2}{\overline{B_{\hat{z}}}}\cos^2\theta \tag{A14}$$

as an enhanced vertical momentum diffusion (as in Greatbatch and Lamb 1990 but modified by the geometric factor $\cos^2\theta$, which approaches unity for shallow slopes).

Although we have shown that the slope-averaged equations can be closed through an enhanced eddy viscosity, the parameterization is incomplete since we have not specified the magnitude or structure of $K(z)$ in terms of only resolved quantities and external parameters.

Developing such a parameterization is beyond the scope of this paper; however, we can explore the impact of such a parameterization by diagnosing the cross-slope eddy flux—and the resulting effective eddy diffusivity (A11)—from the Smooth3D simulation and substituting it back into the corresponding 1D model given by

$$u_t^\dagger - f\overline{v}\cos\theta = \overline{b}\sin\theta + \partial_z\left(\kappa u_z^\dagger\right), \tag{A15}$$

$$\overline{v}_t + fu^\dagger\cos\theta = \partial_z\left(\sigma_v(z)\kappa\overline{v}_z\right), \tag{A16}$$

$$w^\dagger = 0 \tag{A17}$$

$$\overline{p}_z = \overline{b}\cos\theta, \tag{A18}$$

$$\overline{b}_t + u^\dagger N^2\sin\theta = \partial_z\left[\kappa\left(N^2\cos\theta + \overline{b}_z\right)\right]. \tag{A19}$$

This set of equations is identical to the canonical 1D sloping BBL model (8) through (10) for the Eulerian mean circulation except for the enhancement of vertical diffusion of along-slope momentum by a factor $\sigma_v(z)$. Figure 11a shows how the effective vertical Prandtl number can be approximated by a simple vertical structure, $\sigma_v(z) \propto z\exp\{-z/\eta\}$ with an optimal vertical scale of $\eta = 225\,\mathrm{m} \approx h$ and a peak magnitude of $\sigma_v = \mathcal{O}(100)$, dramatically enhancing the vertical diffusion of the along-slope thermal wind. This form satisfies $\sigma_v \to 1$ as $z \to 0$, such that the eddy-induced flow does not interfere with the bottom boundary conditions on the Eulerian mean flow.

Figure 1 and Figures 8a,b,c show the impact of this momentum diffusion on the 1D BBL solution and its buoyancy budget, respectively. Callies (2018) and Holmes et al. (2019) propose conceptually similar parameterizations, but omit the derivation and assume a vertically-uniform enhancement of the Prandtl number $\sigma = 230$, which distorts the vertical structure of submesoscale eddy restratification.

References

Andrews, D. G., and M. E. McIntyre, 1976: Planetary Waves in Horizontal and Vertical Shear: The Generalized Eliassen-Palm Relation and the Mean Zonal Acceleration. *Journal of the Atmospheric Sciences*, **33 (11)**, 2031–2048, doi:10.1175/1520-0469(1976)033⟨2031:PWIHAV⟩2.0.CO;2, publisher: American Meteorological Society.

Armi, L., 1978: Some evidence for boundary mixing in the deep Ocean. *Journal of Geophysical Research*, **83 (C4)**, 1971, doi:10.1029/JC083iC04p01971, URL http://doi.wiley.com/10.1029/JC083iC04p01971.

Armi, L., 1979a: Effects of variations in eddy diffusivity on property distributions in the oceans. *Journal of Marine Research*, **37 (3)**, 515–530, URL https://escholarship.org/uc/item/65g216cr.

Armi, L., 1979b: Reply to Comments by C. Garrett. *Journal of Geophysical Research*, **84 (C8)**, 5097, doi:10.1029/JC084iC08p05097, URL http://doi.wiley.com/10.1029/JC084iC08p05097, publisher: Wiley-Blackwell.

Armi, L., and E. D'Asaro, 1980: Flow structures of the benthic ocean. *Journal of Geophysical Research: Oceans*, **85 (C1)**, 469–484, doi:https://doi.org/10.1029/JC085iC01p00469, URL https://agupubs.onlinelibrary.wiley.com/doi/abs/10.1029/JC085iC01p00469, _eprint: https://agupubs.onlinelibrary.wiley.com/doi/pdf/10.1029/JC085iC01p00469.

Baines, P. G., 1979: Observations of stratified flow past Three-dimensional barriers. *Journal of Geophysical Research: Oceans*, **84 (C12)**, 7834–7838, doi:10.1029/JC084iC12p07834, URL https://agupubs.onlinelibrary.wiley.com/doi/abs/10.1029/JC084iC12p07834, _eprint: https://agupubs.onlinelibrary.wiley.com/doi/pdf/10.1029/JC084iC12p07834.

Boccaletti, G., R. Ferrari, and B. Fox-Kemper, 2007: Mixed Layer Instabilities and Restratification. *Journal of Physical Oceanography*, **37 (9)**, 2228–2250, doi:10.1175/JPO3101.1, URL http://journals.ametsoc.org/doi/abs/10.1175/JPO3101.1.

Bryden, H. L., and A. J. G. Nurser, 2003: Effects of Strait Mixing on Ocean Stratification. *Journal of Physical Oceanography*, **33 (8)**, 1870–1872, doi:10.1175/1520-0485(2003)033⟨1870:EOSMOO⟩2.0.CO;2, URL https://journals.ametsoc.org/view/journals/phoc/33/8/1520-0485_2003_033_1870_eosmoo_2.0.co_2.xml, publisher: American Meteorological Society Section: Journal of Physical Oceanography.

Burns, K. J., G. M. Vasil, J. S. Oishi, D. Lecoanet, and B. Brown, 2016: Dedalus: Flexible framework for spectrally solving differential equations. *Astrophysics Source Code Library, record ascl:1603.015*, URL http://adsabs.harvard.edu/abs/2016ascl.soft03015B.

Cael, B., and A. Mashayek, 2021: Log-Skew-Normality of Ocean Turbulence. *Physical Review Letters*, **126 (22)**, 224 502, doi:10.1103/PhysRevLett.126.224502, URL https://link.aps.org/doi/10.1103/PhysRevLett.126.224502, publisher: American Physical Society.

Callies, J., 2018: Restratification of Abyssal Mixing Layers by Submesoscale Baroclinic Eddies. *Journal of Physical Oceanography*, JPO–D–18–0082.1, doi:10.1175/JPO-D-18-0082.1, URL http://journals.ametsoc.org/doi/10.1175/JPO-D-18-0082.1.

Callies, J., and R. Ferrari, 2018: Dynamics of an Abyssal Circulation Driven by Bottom-Intensified Mixing on Slopes. *Journal of Physical Oceanography*, **48 (6)**, 1257–1282, doi:10.1175/JPO-D-17-0125.1, URL http://journals.ametsoc.org/doi/10.1175/JPO-D-17-0125.1.

Cimoli, L., C.-c. P. Caulfield, H. L. Johnson, D. P. Marshall, A. Mashayek, A. C. N. Garabato, and C. Vic, 2019: Sensitivity of deep ocean mixing to local internal tide breaking and mixing efficiency. *Geophysical Research Letters*, **n/a (n/a)**, doi:10.1029/2019GL085056, URL https://agupubs.onlinelibrary.wiley.com/doi/abs/10.1029/2019GL085056.

Clément, L., A. M. Thurnherr, and L. C. St. Laurent, 2017: Turbulent Mixing in a Deep Fracture Zone on the Mid-Atlantic Ridge. *Journal of Physical Oceanography*, **47 (8)**, 1873–1896, doi:10.1175/JPO-D-16-0264.1, URL http://journals.ametsoc.org/doi/10.1175/JPO-D-16-0264.1.

de Lavergne, C., G. Madec, J. Le Sommer, A. J. G. Nurser, and A. C. Naveira Garabato, 2016: On the Consumption of Antarctic Bottom Water in the Abyssal Ocean. *Journal of Physical Oceanography*, **46 (2)**, 635–661, doi:10.1175/JPO-D-14-0201.1, URL http://journals.ametsoc.org/doi/10.1175/JPO-D-14-0201.1.

de Lavergne, C., and Coauthors, 2020: A Parameterization of Local and Remote Tidal Mixing. *Journal of Advances in Modeling Earth Systems*, **12 (5)**, e2020MS002 065, doi:https://doi.org/10.1029/2020MS002065, URL https://agupubs.onlinelibrary.wiley.com/doi/abs/10.1029/2020MS002065, _eprint: https://agupubs.onlinelibrary.wiley.com/doi/pdf/10.1029/2020MS002065.

Dell, R., and L. Pratt, 2015: Diffusive boundary layers over varying topography. *Journal of Fluid Mechanics*, **769**, 635–653, doi:10.1017/jfm.2015.88, URL http://www.journals.cambridge.org/abstract_S0022112015000889.

Dell, R. W., 2013: *Boundary layer dynamics and deep ocean mixing in Mid-Atlantic Ridge canyons*. Massachusetts Institute of Technology and Woods Hole Oceanographic Institution, Woods Hole, MA, doi:10.1575/1912/5740, URL https://hdl.handle.net/1912/5740.

Drake, H. F., 2021: Control of the abyssal ocean overturning circulation by mixing-driven bottom boundary layers. Thesis, Massachusetts Institute of Technology and Woods Hole Oceanographic Institution, doi:10.1575/1912/27424, URL https://darchive.mblwhoilibrary.org/handle/1912/27424, accepted: 2021-08-10T15:07:15Z.

Drake, H. F., R. Ferrari, and J. Callies, 2020: Abyssal Circulation Driven by Near-Boundary Mixing: Water Mass Transformations and Interior Stratification. *Journal of Physical Oceanography*, **50 (8)**, 2203–2226, doi:10.1175/JPO-D-19-0313.1, URL https://journals.ametsoc.org/jpo/article/50/8/2203/348530/Abyssal-Circulation-Driven-by-Near-Boundary-Mixing, publisher: American Meteorological Society.

Drake, H. F., X. Ruan, and R. Ferrari, 2022: Diapycnal motion, diffusion, and stretching of tracers in the ocean. URL https://eartharxiv.org/repository/view/3001/, publisher: EarthArXiv.

Ferrari, R., 2014: What goes down must come up. *Nature*, **513**, 179–180.

Ferrari, R., A. Mashayek, T. J. McDougall, M. Nikurashin, and J.-M. Campin, 2016: Turning Ocean Mixing Upside Down. *Journal of Physical Oceanography*, **46 (7)**, 2239–2261, doi:10.1175/JPO-D-15-0244.1, URL http://journals.ametsoc.org/doi/10.1175/JPO-D-15-0244.1.

Ferrari, R., and R. Plumb, 2003: Residual circulation in the ocean. *Near-Boundary Processes and Their Parameterization: Proc.'Aha Huliko'a Hawaiian Winter Workshop*, 219–228.

Ferron, B., H. Mercier, K. Speer, A. Gargett, and K. Polzin, 1998: Mixing in the Romanche Fracture Zone. *Journal of Physical Oceanography*, **28 (10)**, 1929–1945, doi:10.1175/

1520-0485(1998)028⟨1929:MITRFZ⟩2.0.CO;2, URL https://journals.ametsoc.org/view/journals/phoc/28/10/1520-0485_1998_028_1929_mitrfz_2.0.co_2.xml, publisher: American Meteorological Society Section: Journal of Physical Oceanography.

Fox-Kemper, B., R. Ferrari, and R. Hallberg, 2008: Parameterization of Mixed Layer Eddies. Part I: Theory and Diagnosis. *Journal of Physical Oceanography*, **38 (6)**, 1145–1165, doi:10.1175/2007JPO3792.1, URL http://journals.ametsoc.org/doi/abs/10.1175/2007JPO3792.1.

Garrett, C., 1979: Comment on 'Some evidence for boundary mixing in the deep ocean' by Laurence Armi. *Journal of Geophysical Research*, **84 (C8)**, 5095, doi:10.1029/JC084iC08p05095, URL http://doi.wiley.com/10.1029/JC084iC08p05095, publisher: Wiley-Blackwell.

Garrett, C., 1990: The role of secondary circulation in boundary mixing. *Journal of Geophysical Research*, **95 (C3)**, 3181, doi:10.1029/JC095iC03p03181, URL http://doi.wiley.com/10.1029/JC095iC03p03181, publisher: Wiley-Blackwell.

Garrett, C., P. MacCready, and P. Rhines, 1993: Boundary Mixing and Arrested Ekman Layers: Rotating Stratified Flow Near a Sloping Boundary. *Annual Review of Fluid Mechanics*, **25 (1)**, 291–323, doi:10.1146/annurev.fl.25.010193.001451, URL http://www.annualreviews.org/doi/10.1146/annurev.fl.25.010193.001451, publisher: Annual Reviews 4139 El Camino Way, P.O. Box 10139, Palo Alto, CA 94303-0139, USA.

Gayen, B., and S. Sarkar, 2011: Negative turbulent production during flow reversal in a stratified oscillating boundary layer on a sloping bottom. *Physics of Fluids*, **23 (10)**, 101 703, doi:10.1063/1.3651359, URL https://aip.scitation.org/doi/10.1063/1.3651359, publisher: American Institute of Physics.

Gent, P. R., and J. C. McWilliams, 1990: Isopycnal Mixing in Ocean Circulation Models. *Journal of Physical Oceanography*, **20 (1)**, 150–155, doi:10.1175/1520-0485(1990)020⟨0150:IMIOCM⟩2.0.CO;2, URL http://journals.ametsoc.org/doi/abs/10.1175/1520-0485(1990)020%3C0150:IMIOCM%3E2.0.CO;2, iSBN: 0022-3670.

Gent, P. R., J. Willebrand, T. J. McDougall, and J. C. McWilliams, 1995: Parameterizing Eddy-Induced Tracer Transports in Ocean Circulation Models. *Journal of Physical Oceanography*, **25 (4)**, 463–474, doi:10.1175/1520-0485(1995)025⟨0463:PEITTI⟩2.0.CO;2, URL https://journals.ametsoc.org/view/journals/phoc/25/4/1520-0485_1995_025_0463_peitti_2_0_co_2.xml, publisher: American Meteorological Society Section: Journal of Physical Oceanography.

Gordon, A. L., 1986: Is there a global scale ocean circulation? *Eos, Transactions American Geophysical Union*, **67 (9)**, 109–110, doi:https://doi.org/10.1029/EO067i009p00109, URL https://agupubs.onlinelibrary.wiley.com/doi/abs/10.1029/EO067i009p00109, _eprint: https://agupubs.onlinelibrary.wiley.com/doi/pdf/10.1029/EO067i009p00109.

Greatbatch, R. J., and K. G. Lamb, 1990: On Parameterizing Vertical Mixing of Momentum in Non-eddy Resolving Ocean Models. *Journal of Physical Oceanography*, **20 (10)**, 1634–1637, doi:10.1175/1520-0485(1990)020⟨1634:OPVMOM⟩2.0.CO;2, URL https://journals.ametsoc.org/doi/abs/10.1175/1520-0485%281990%29020%3C1634%3AOPVMOM%3E2.0.CO%3B2.

Gregg, M., E. D'Asaro, J. Riley, and E. Kunze, 2018: Mixing Efficiency in the Ocean. *Annual Review of Marine Science*, **10 (1)**, 443–473, doi:10.1146/annurev-marine-121916-063643, URL http://www.annualreviews.org/doi/10.1146/annurev-marine-121916-063643.

Gregg, M. C., 1987: Diapycnal mixing in the thermocline: A review. *Journal of Geophysical Research*, **92 (C5)**, 5249, doi:10.1029/JC092iC05p05249, URL http://doi.wiley.com/10.1029/JC092iC05p05249.

Held, I. M., 2005: The gap between simulation and understanding in climate modeling. *Bulletin of the American Meteorological Society*, **86 (11)**, 1609–1614, doi:10.1175/BAMS-86-11-1609, iSBN: 0003-0007.

Hogg, N., P. Biscaye, W. Gardner, and W. Jr, 1982: On the Transport and Modification of Antarctic Bottom Water in the Vema Channel. *J. Mar. Res.*, **40**, 231–263.

Holmes, R. M., C. de Lavergne, and T. J. McDougall, 2018: Ridges, Seamounts, Troughs, and Bowls: Topographic Control of the Dianeutral Circulation in the Abyssal Ocean. *Journal of Physical Oceanography*, **48 (4)**, 861–882, doi:10.1175/JPO-D-17-0141.1, URL http://journals.ametsoc.org/doi/10.1175/JPO-D-17-0141.1.

Holmes, R. M., C. de Lavergne, and T. J. McDougall, 2019: Tracer Transport within Abyssal Mixing Layers. *Journal of Physical Oceanography*, **49 (10)**, 2669–2695, doi:10.1175/JPO-D-19-0006.1, URL https://journals.ametsoc.org/doi/full/10.1175/JPO-D-19-0006.1, publisher: American Meteorological Society.

Holmes, R. M., and T. J. McDougall, 2020: Diapycnal Transport near a Sloping Bottom Boundary. *Journal of Physical Oceanography*, **50 (11)**, 3253–3266, doi:10.1175/JPO-D-20-0066.1, URL https://journals.ametsoc.org/view/journals/phoc/50/11/jpoD200066.xml, publisher: American Meteorological Society Section: Journal of Physical Oceanography.

Hoyer, S., and J. Hamman, 2017: xarray: N-D labeled arrays and datasets in Python. *Journal of Open Research Software*, **5 (1)**, doi:10.5334/jors.148, URL http://doi.org/10.5334/jors.148.

Huang, R. X., and X. Jin, 2002: Deep Circulation in the South Atlantic Induced by Bottom-Intensified Mixing over the Midocean Ridge*. *Journal of Physical Oceanography*, **32 (4)**, 1150–1164, doi:10.1175/1520-0485(2002)032⟨1150:DCITSA⟩2.0.CO;2.

Ijichi, T., L. S. Laurent, K. L. Polzin, and J. M. Toole, 2020: How Variable Is Mixing Efficiency in the Abyss? *Geophysical Research Letters*, **47 (7)**, e2019GL086 813, doi:10.1029/2019GL086813, URL https://agupubs.onlinelibrary.wiley.com/doi/abs/10.1029/2019GL086813, _eprint: https://agupubs.onlinelibrary.wiley.com/doi/pdf/10.1029/2019GL086813.

Kaiser, B. E., 2020: Finescale abyssal turbulence : sources and modeling. Thesis, Massachusetts Institute of Technology, URL https://dspace.mit.edu/handle/1721.1/128078, accepted: 2020-10-18T21:45:36Z.

Kunze, E., 2017: The Internal-Wave-Driven Meridional Overturning Circulation. *Journal of Physical Oceanography*, **47 (11)**, 2673–2689, doi:10.1175/JPO-D-16-0142.1, URL http://journals.ametsoc.org/doi/10.1175/JPO-D-16-0142.1.

Kunze, E., E. Firing, J. M. Hummon, T. K. Chereskin, and A. M. Thurnherr, 2006: Global Abyssal Mixing Inferred from Lowered ADCP Shear and CTD Strain Profiles. *Journal of Physical Oceanography*, **36 (8)**, 1553–1576, doi:10.1175/JPO2926.1, URL https://journals.ametsoc.org/view/journals/phoc/36/8/jpo2926.1.xml, publisher: American Meteorological Society Section: Journal of Physical Oceanography.

Kunze, E., C. MacKay, E. E. McPhee-Shaw, K. Morrice, J. B. Girton, and S. R. Terker, 2012: Turbulent Mixing and Exchange with Interior Waters on Sloping Boundaries. *Journal of Physical Oceanography*, **42 (6)**, 910–927, doi:10.1175/JPO-D-11-075.1, URL http://journals.ametsoc.org/doi/abs/10.1175/JPO-D-11-075.1.

Ledwell, J. R., E. T. Montgomery, K. L. Polzin, L. C. St. Laurent, R. W. Schmitt, and J. M. Toole, 2000: Evidence for enhanced mixing over rough topography in the abyssal ocean. *Nature*, **403 (6766)**, 179–182, doi:10.1038/35003164, URL http://www.nature.com/articles/35003164, publisher: Nature Publishing Group.

Ledwell, J. R., A. J. Watson, and C. S. Law, 1993: Evidence for slow mixing across the pycnocline from an open-ocean tracer-release experiment. *Nature*, **364 (6439)**, 701–703, doi:10.1038/364701a0, URL http://www.nature.com/doifinder/10.1038/364701a0, publisher: Nature Publishing Group.

Legg, S., and Coauthors, 2009: Improving Oceanic Overflow Representation in Climate Models: The Gravity Current Entrainment Climate Process Team. *Bulletin of the American Meteorological Society*, **90 (5)**, 657–670, doi:10.1175/2008BAMS2667.1, URL https://journals.ametsoc.org/view/journals/bams/90/5/2008bams2667_1.xml, publisher: American Meteorological Society Section: Bulletin of the American Meteorological Society.

MacCready, P., and P. B. Rhines, 1991: Buoyant inhibition of Ekman transport on a slope and its effect on stratified spin-up. *Journal of Fluid Mechanics*, **223 (-1)**, 631, doi:10.1017/S0022112091001581, URL http://www.journals.cambridge.org/abstract_S0022112091001581, publisher: Cambridge University Press.

Marshall, J., C. Hill, L. Perelman, and A. Adcroft, 1997: Hydrostatic, quasi-hydrostatic, and nonhydrostatic ocean modeling. *Journal of Geophysical Research*, **102 (C3)**, 5733, doi:10.1029/96JC02776, iSBN: 2156-2202.

Marshall, J., and T. Radko, 2003: Residual-Mean Solutions for the Antarctic Circumpolar Current and Its Associated Overturning Circulation. *Journal of Physical Oceanography*, **33 (11)**, 2341–2354, doi:10.1175/1520-0485(2003)033⟨2341:RSFTAC⟩2.0.CO;2, URL http://dx.doi.org/10.1175/1520-0485(2003)033%3C2341:RSFTAC%3E2.0.CO;2, iSBN: 0022-3670.

Mashayek, A., J. Gula, L. Baker, A. N. Garabato, L. Cimoli, and J. Riley, 2021: Mountains to climb: on the role of seamounts in upwelling of deep ocean water. Tech. rep. doi:10.21203/rs.3.rs-939198/v1, URL https://doi.org/10.21203/rs.3.rs-939198/v1, type: article.

McDougall, T. J., and R. Ferrari, 2017: Abyssal Upwelling and Downwelling Driven by Near-Boundary Mixing. *Journal of Physical Oceanography*, **47 (2)**, 261–283, doi:10.1175/JPO-D-16-0082.1, URL https://journals.ametsoc.org/doi/full/10.1175/JPO-D-16-0082.1, publisher: American Meteorological Society.

Melet, A., R. Hallberg, S. Legg, and M. Nikurashin, 2014: Sensitivity of the Ocean State to Lee Wave–Driven Mixing. *Journal of Physical Oceanography*, **44 (3)**, 900–921, doi:10.1175/JPO-D-13-072.1, URL http://journals.ametsoc.org/doi/abs/10.1175/JPO-D-13-072.1.

Morris, M. Y., M. M. Hall, L. C. S. Laurent, and N. G. Hogg, 2001: Abyssal Mixing in the Brazil Basin. *Journal of Physical Oceanography*, **31 (11)**, 3331–3348, doi:10.1175/1520-0485(2001)031⟨3331:AMITBB⟩2.0.CO;2, URL https://journals.ametsoc.org/view/

journals/phoc/31/11/1520-0485_2001_031_3331_amitbb_2.0.co_2.xml, publisher: American Meteorological Society Section: Journal of Physical Oceanography.

Munk, W. H., 1966: Abyssal recipes. *Deep Sea Research and Oceanographic Abstracts*, **13 (4)**, 707–730, doi:10.1016/0011-7471(66)90602-4, arXiv: cs/9605103 ISBN: 1600117471.

Naveira Garabato, A. C., and Coauthors, 2019: Rapid mixing and exchange of deep-ocean waters in an abyssal boundary current. *Proceedings of the National Academy of Sciences*, **116 (27)**, 13 233–13 238, doi:10.1073/pnas.1904087116, URL https://www.pnas.org/content/116/27/13233, iSBN: 9781904087113 Publisher: National Academy of Sciences Section: Physical Sciences.

Nazarian, R. H., C. M. Burns, S. Legg, M. C. Buijsman, H. Kaur, and B. K. Arbic, 2021: On the Magnitude of Canyon-Induced Mixing. *Journal of Geophysical Research: Oceans*, **126 (11)**, e2021JC017 671, doi:10.1029/2021JC017671, URL https://onlinelibrary.wiley.com/doi/abs/10.1029/2021JC017671, _eprint: https://onlinelibrary.wiley.com/doi/pdf/10.1029/2021JC017671.

Nikurashin, M., and R. Ferrari, 2013: Overturning circulation driven by breaking internal waves in the deep ocean. *Geophysical Research Letters*, **40 (12)**, 3133–3137, doi:10.1002/grl.50542, URL http://doi.wiley.com/10.1002/grl.50542, publisher: Wiley-Blackwell.

Nikurashin, M., and S. Legg, 2011: A Mechanism for Local Dissipation of Internal Tides Generated at Rough Topography. *Journal of Physical Oceanography*, **41 (2)**, 378–395, doi:10.1175/2010JPO4522.1, URL http://journals.ametsoc.org/doi/abs/10.1175/2010JPO4522.1.

Peterson, H. G., and J. Callies, 2021: Rapid spin up and spin down of flow along slopes. *Journal of Physical Oceanography*, **-1 (aop)**, doi:10.1175/JPO-D-21-0173.1, URL https://journals.ametsoc.org/view/journals/phoc/aop/JPO-D-21-0173.1/JPO-D-21-0173.1.xml, publisher: American Meteorological Society Section: Journal of Physical Oceanography.

Phillips, O., 1970: On flows induced by diffusion in a stably stratified fluid. *Deep Sea Research and Oceanographic Abstracts*, **17 (3)**, 435–443, doi:10.1016/0011-7471(70)90058-6, URL http://linkinghub.elsevier.com/retrieve/pii/0011747170900586.

Plumb, R. A., and R. Ferrari, 2005: Transformed Eulerian-Mean Theory. Part I: Nonquasi-geostrophic Theory for Eddies on a Zonal-Mean Flow. *Journal of Physical Oceanography*, **35 (2)**, 165–174, doi:10.1175/JPO-2669.1, URL http://journals.ametsoc.org/doi/abs/10.1175/JPO-2669.1.

Polzin, K., J. Toole, J. R. Ledwell, and R. Schmitt, 1997: Spatial Variability of Turbulent Mixing in the Spatial Variability Abyssal Ocean. *Science*, **276 (5309)**, 93–96, doi:10.1126/science.276.5309.93, URL http://www.sciencemag.org/cgi/content/abstract/276/5309/93, iSBN: 0036-8075.

Polzin, K. L., 2009: An abyssal recipe. *Ocean Modelling*, **30 (4)**, 298–309, doi:10.1016/j.ocemod.2009.07.006.

Polzin, K. L., and T. J. McDougall, 2022: Chapter 7 - Mixing at the ocean's bottom boundary. *Ocean Mixing*, M. Meredith, and A. Naveira Garabato, Eds., Elsevier, 145–180, doi:10.1016/B978-0-12-821512-8.00014-1, URL https://www.sciencedirect.com/science/article/pii/B9780128215128000141.

Polzin, K. L., B. Wang, Z. Wang, F. Thwaites, and A. J. Williams, 2021: Moored Flux and Dissipation Estimates from the Northern Deepwater Gulf of Mexico. *Fluids*, **6 (7)**, 237, doi:10.3390/fluids6070237, URL https://www.mdpi.com/2311-5521/6/7/237, number: 7 Publisher: Multidisciplinary Digital Publishing Institute.

Pratt, L., and J. Whitehead, 2008: *Rotating Hydraulics: Nonlinear Topographic Effects in the Ocean and Atmosphere.*

Rhines, P. B., and W. R. Young, 1982: Homogenization of potential vorticity in planetary gyres. *Journal of Fluid Mechanics*, **122**, 347–367, doi:10.1017/S0022112082002250, URL https://www.cambridge.org/core/journals/journal-of-fluid-mechanics/article/abs/homogenization-of-potential-vorticity-in-planetary-gyres/D4A576A163DA70D49957DF1FA5DB2708, publisher: Cambridge University Press.

Ruan, X., and J. Callies, 2020: Mixing-Driven Mean Flows and Submesoscale Eddies over Mid-Ocean Ridge Flanks and Fracture Zone Canyons. *Journal of Physical Oceanography*, **50 (1)**, 175–195, doi:10.1175/JPO-D-19-0174.1, URL https://journals.ametsoc.org/view/journals/phoc/50/1/jpo-d-19-0174.1.xml, publisher: American Meteorological Society Section: Journal of Physical Oceanography.

Salmun, H., P. D. Killworth, and J. R. Blundell, 1991: A two-dimensional model of boundary mixing. *Journal of Geophysical Research: Oceans*, **96 (C10)**, 18 447–18 474, doi:10.1029/91JC01917, URL https://agupubs.onlinelibrary.wiley.com/doi/abs/10.1029/91JC01917.

Smith, W. H. F., and D. T. Sandwell, 1997: Global Sea Floor Topography from Satellite Altimetry and Ship Depth Soundings. *Science*, **277 (5334)**, 1956–1962, doi:10.1126/science.277.5334.1956, URL https://science.sciencemag.org/content/277/5334/1956, publisher: American Association for the Advancement of Science Section: Research Article.

Spingys, C. P., A. C. N. Garabato, S. Legg, K. L. Polzin, E. P. Abrahamsen, C. E. Buckingham, A. Forryan, and E. E. Frajka-Williams, 2021: Mixing and Transformation in a Deep Western Boundary Current: A Case Study. *Journal of Physical Oceanography*, **51 (4)**, 1205–1222, doi:10.1175/JPO-D-20-0132.1, URL https://journals.ametsoc.org/view/journals/phoc/aop/JPO-D-20-0132.1/JPO-D-20-0132.1.xml, publisher: American Meteorological Society Section: Journal of Physical Oceanography.

St. Laurent, L., and C. Garrett, 2002: The Role of Internal Tides in Mixing the Deep Ocean. *Journal of Physical Oceanography*, **32 (10)**, 2882–2899, doi:10.1175/1520-0485(2002)032⟨2882:TROITI⟩2.0.CO;2, URL http://journals.ametsoc.org/doi/abs/10.1175/1520-0485%282002%29032%3C2882%3ATROITI%3E2.0.CO%3B2.

St. Laurent, L. C., J. M. Toole, and R. W. Schmitt, 2001: Buoyancy Forcing by Turbulence above Rough Topography in the Abyssal Brazil Basin*. *Journal of Physical Oceanography*, **31 (12)**, 3476–3495, doi:10.1175/1520-0485(2001)031⟨3476:BFBTAR⟩2.0.CO;2.

Stommel, H., 1958: The abyssal circulation. *Deep Sea Research (1953)*, **5 (1)**, 80–82, doi:10.1016/S0146-6291(58)80014-4, URL https://www.sciencedirect.com/science/article/pii/S0146629158800144.

Stone, P. H., 1966: On Non-Geostrophic Baroclinic Stability. *Journal of the Atmospheric Sciences*, **23 (4)**, 390–400, doi:10.1175/1520-0469(1966)023⟨0390:ONGBS⟩2.0.CO;2, URL https://journals.ametsoc.org/view/journals/atsc/23/4/1520-0469_1966_023_0390_ongbs_2_0_co_2.xml, publisher: American Meteorological Society Section: Journal of the Atmospheric Sciences.

Sverdrup, H., M. Johnson, and R. Fleming, 1942: The Oceans: Their Physics, Chemistry and General Biology. *Oceanography*, 1104, doi:10.2307/210609, arXiv: 1011.1669v3 ISBN: 9788578110796.

Talley, L. D., 2013: Closure of the Global Overturning Circulation Through the Indian, Pacific, and Southern Oceans: Schematics and Transports. *Oceanography*, **26 (1)**, 80–97, doi:10.5670/oceanog.2013.07, URL http://apps.webofknowledge.com/full_record.do?product=UA&search_mode=GeneralSearch&qid=14&SID=W1jPgx8kkS6brME6NvD&page=1&doc=1, arXiv: 1011.1669v3 ISBN: 1042-8275.

Talley, L. D., J. L. Reid, and P. E. Robbins, 2003: Data-Based Meridional Overturning Streamfunctions for the Global Ocean. *Journal of Climate*, **16 (19)**, 3213–3226, doi:10.1175/1520-0442(2003)016⟨3213:DMOSFT⟩2.0.CO;2, URL https://journals.ametsoc.org/view/journals/clim/16/19/1520-0442_2003_016_3213_dmosft_2.0.co_2.xml, publisher: American Meteorological Society Section: Journal of Climate.

Taylor, G. I., and W. N. Shaw, 1920: I. Tidal friction in the Irish Sea. *Philosophical Transactions of the Royal Society of London. Series A, Containing Papers of a Mathematical or Physical Character*, **220 (571-581)**, 1–33, doi:10.1098/rsta.1920.0001, URL https://royalsocietypublishing.org/doi/10.1098/rsta.1920.0001, publisher: Royal Society.

Thompson, L., and G. C. Johnson, 1996: Abyssal currents generated by diffusion and geothermal heating over rises. *Deep Sea Research Part I: Oceanographic Research Papers*, **43 (2)**, 193–211, doi:10.1016/0967-0637(96)00095-7, URL http://www.sciencedirect.com/science/article/pii/0967063796000957.

Thorpe, S. A., 1987: Current and Temperature Variability on the Continental Slope. *Philosophical Transactions of the Royal Society A: Mathematical, Physical and Engi-*

neering Sciences, **323 (1574)**, 471–517, doi:10.1098/rsta.1987.0100, URL http://rsta.royalsocietypublishing.org/cgi/doi/10.1098/rsta.1987.0100, publisher: The Royal Society.

Thorpe, S. A., 2005: *The Turbulent Ocean*. Cambridge University Press, Cambridge, doi:10.1017/CBO9780511819933, URL https://www.cambridge.org/core/books/turbulent-ocean/1F9A34350F4AA077CA27641C6884B61B.

Thurnherr, A. M., 2000: Hydrography and flow in the rift valley of the Mid-Atlantic Ridge. phd, University of Southampton, URL https://eprints.soton.ac.uk/42174/.

Thurnherr, A. M., L. Clément, L. S. Laurent, R. Ferrari, and T. Ijichi, 2020: Transformation and Upwelling of Bottom Water in Fracture Zone Valleys. *Journal of Physical Oceanography*, **50 (3)**, 715–726, doi:10.1175/JPO-D-19-0021.1, URL https://journals.ametsoc.org/view/journals/phoc/50/3/jpo-d-19-0021.1.xml, publisher: American Meteorological Society Section: Journal of Physical Oceanography.

Thurnherr, A. M., and K. G. Speer, 2003: Boundary Mixing and Topographic Blocking on the Mid-Atlantic Ridge in the South Atlantic*. *Journal of Physical Oceanography*, **33 (4)**, 848–862, doi:10.1175/1520-0485(2003)33⟨848:BMATBO⟩2.0.CO;2, URL http://journals.ametsoc.org/doi/abs/10.1175/1520-0485%282003%2933%3C848%3ABMATBO%3E2.0.CO%3B2.

Thurnherr, A. M., and Coauthors, 2005: Mixing Associated with Sills in a Canyon on the Midocean Ridge Flank*. *Journal of Physical Oceanography*, **35 (8)**, 1370–1381, doi:10.1175/JPO2773.1, URL http://journals.ametsoc.org/doi/abs/10.1175/JPO2773.1.

Toole, J. M., 2007: Temporal Characteristics of Abyssal Finescale Motions above Rough Bathymetry. *Journal of Physical Oceanography*, **37 (3)**, 409–427, doi:10.1175/JPO2988.

1, URL https://journals.ametsoc.org/view/journals/phoc/37/3/jpo2988.1.xml, publisher: American Meteorological Society Section: Journal of Physical Oceanography.

Tozer, B., D. T. Sandwell, W. H. F. Smith, C. Olson, J. R. Beale, and P. Wessel, 2019: Global Bathymetry and Topography at 15 Arc Sec: SRTM15+. *Earth and Space Science*, **6 (10)**, 1847–1864, doi:10.1029/2019EA000658, URL https://agupubs.onlinelibrary.wiley.com/doi/abs/10.1029/2019EA000658, _eprint: https://agupubs.onlinelibrary.wiley.com/doi/pdf/10.1029/2019EA000658.

Tziperman, E., 1986: On the Role of Interior Mixing and Air-Sea Fluxes in Determining the Stratification and Circulation of the Oceans. *Journal of Physical Oceanography*, **16 (4)**, 680–693, doi:10.1175/1520-0485(1986)016⟨0680:OTROIM⟩2.0.CO;2, URL https://journals.ametsoc.org/view/journals/phoc/16/4/1520-0485_1986_016_0680_otroim_2_0_co_2.xml, publisher: American Meteorological Society Section: Journal of Physical Oceanography.

van Haren, H., 2018: High-Resolution Observations of Internal Wave Turbulence in the Deep Ocean. *The Ocean in Motion: Circulation, Waves, Polar Oceanography*, M. G. Velarde, R. Y. Tarakanov, and A. V. Marchenko, Eds., Springer Oceanography, Springer International Publishing, Cham, 127–146, doi:10.1007/978-3-319-71934-4_11, URL https://doi.org/10.1007/978-3-319-71934-4_11.

Voet, G., J. B. Girton, M. H. Alford, G. S. Carter, J. M. Klymak, and J. B. Mickett, 2015: Pathways, Volume Transport, and Mixing of Abyssal Water in the Samoan Passage. *Journal of Physical Oceanography*, **45 (2)**, 562–588, doi:10.1175/JPO-D-14-0096.1, URL https://journals.ametsoc.org/view/journals/phoc/45/2/jpo-d-14-0096.1.xml, publisher: American Meteorological Society Section: Journal of Physical Oceanography.

Walin, G., 1982: On the relation between sea-surface heat flow and thermal circulation in the ocean. *Tellus*, **34 (2)**, 187–195, doi:10.3402/tellusa.v34i2.10801, URL https://doi.org/10.3402/tellusa.v34i2.10801.

Watson, A. J., J. R. Ledwell, D. J. Webb, and C. Wunsch, 1988: Purposefully Released Tracers [and Discussion]. *Philosophical Transactions of the Royal Society of London. Series A, Mathematical and Physical Sciences*, **325 (1583)**, 189–200, URL https://www.jstor.org/stable/38109, publisher: The Royal Society.

Wenegrat, J. O., J. Callies, and L. N. Thomas, 2018: Submesoscale Baroclinic Instability in the Bottom Boundary Layer. *Journal of Physical Oceanography*, JPO–D–17–0264.1, doi:10.1175/JPO-D-17-0264.1, URL http://journals.ametsoc.org/doi/10.1175/JPO-D-17-0264.1.

Whalen, C. B., 2021: Best Practices for Comparing Ocean Turbulence Measurements across Spatiotemporal Scales. *Journal of Atmospheric and Oceanic Technology*, **38 (4)**, 837–841, doi:10.1175/JTECH-D-20-0175.1, URL https://journals.ametsoc.org/view/journals/atot/38/4/JTECH-D-20-0175.1.xml, publisher: American Meteorological Society Section: Journal of Atmospheric and Oceanic Technology.

Whalen, C. B., C. de Lavergne, A. C. Naveira Garabato, J. M. Klymak, J. A. MacKinnon, and K. L. Sheen, 2020: Internal wave-driven mixing: governing processes and consequences for climate. *Nature Reviews Earth & Environment*, **1 (11)**, 606–621, doi:10.1038/s43017-020-0097-z, URL https://www.nature.com/articles/s43017-020-0097-z, number: 11 Publisher: Nature Publishing Group.

Winters, K. B., and L. Armi, 2012: Hydraulic control of continuously stratified flow over an obstacle. *Journal of Fluid Mechanics*, **700**, 502–513, doi:10.1017/jfm.2012.157, URL https://www.cambridge.org/core/journals/journal-of-fluid-mechanics/article/abs/hydraulic-control-of-continuously-stratified-flow-over-an-obstacle/0A67346BF37CCAE5EFACC92238FD92CA, publisher: Cambridge University Press.

Wunsch, C., 1970: On oceanic boundary mixing. *Deep-Sea Research and Oceanographic Abstracts*, **17 (2)**, 293–301, doi:10.1016/0011-7471(70)90022-7.

Young, W. R., 2011: An Exact Thickness-Weighted Average Formulation of the Boussinesq Equations. *Journal of Physical Oceanography*, **42 (5)**, 692–707, doi:10.1175/JPO-D-11-0102.1, URL https://journals.ametsoc.org/doi/full/10.1175/JPO-D-11-0102.1.

LIST OF FIGURES

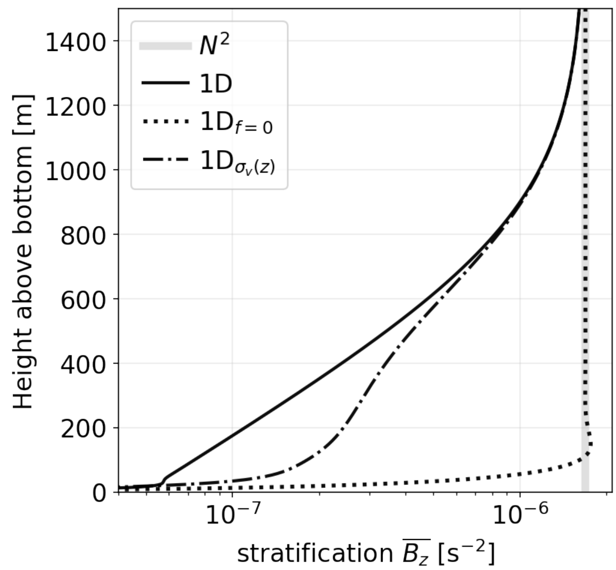

Fig. 1. Height above bottom stratification profiles at steady state for 1D BBL models: with the same external parameters as the BBTRE simulations (solid), without rotation ($f = 0$; dotted), and with enhanced vertical diffusion of along-slope momentum, $\sigma_v(z) \gg 1$ (dash-dotted; see Appendix).

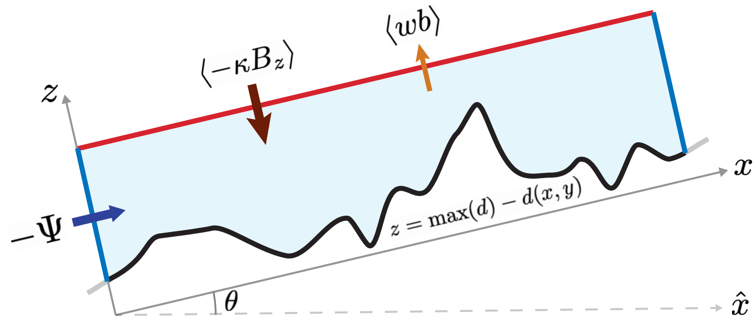

FIG. 2. A generalized slope-normal buoyancy budget (16), derived by integrating the buoyancy equation below a given height above the mean slope z (volume shown in light blue); at equilibrium, the mean up-slope transport (across the background stratification N^2) into the box (blue lines) is given by the net flux of buoyancy into the box from above (red line), $\Psi \propto -\langle -\kappa B_z \rangle - \langle wb \rangle$. We assume no buoyancy flux across the seafloor (black line) at $z = \max(d) - d(x, y)$.

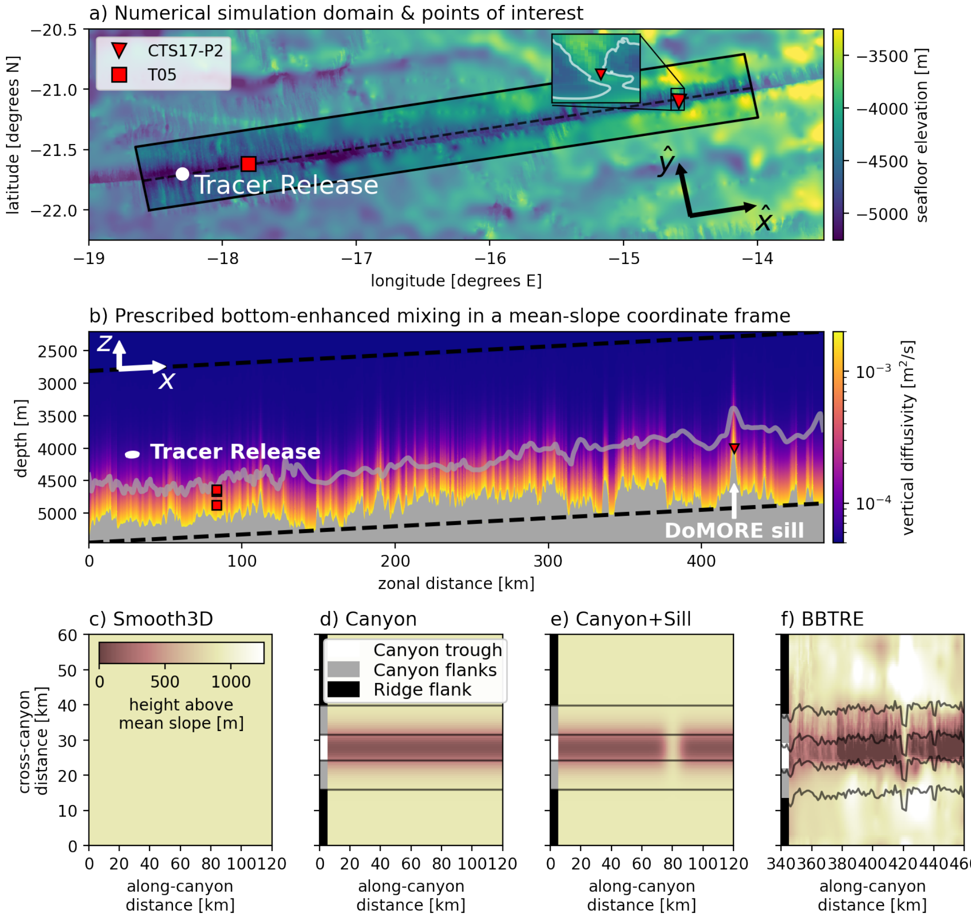

1308 FIG. 3. Numerical model domains. (a) Seafloor elevation $-\hat{d}(\hat{x}, \hat{y})$, including the doubly-periodic simulation domain centered on the Brazil Basin Tracer Release Experiment (BBTRE) canyon. Red markers show the locations of moorings from Clément et al. (2017) (CTS17) and Thurnherr et al. (2005) (T05). The inset highlights the DoMORE sill that dramatically constrains up-canyon flow. White markers mark the injection location from the BBTRE (Ledwell et al. 2000). (b) Imposed slope-normal diffusivity field, the result of applying a self-similar exponential profile as a function of the height-above-bottom (eq. 17) to variable topography. Arrows show the original along-canyon $\hat{\mathbf{y}}$ and cross-canyon $\hat{\mathbf{x}}$ directions as well as the transformed slope-normal $\mathbf{z}$ and along-canyon $\mathbf{x}$ coordinate vectors (a), which appear distorted because the vertical dimension is exaggerated (b). (c-f) A hierarchy of simulations with progressively complex seafloor bathymetry geometries (relative to a constant mean slope of angle θ; see dashed lines in panel b). Thin black lines distinguish three sub-regions: the canyon trough, the canyon's flanks, and the ridge flank surrounding the canyon.

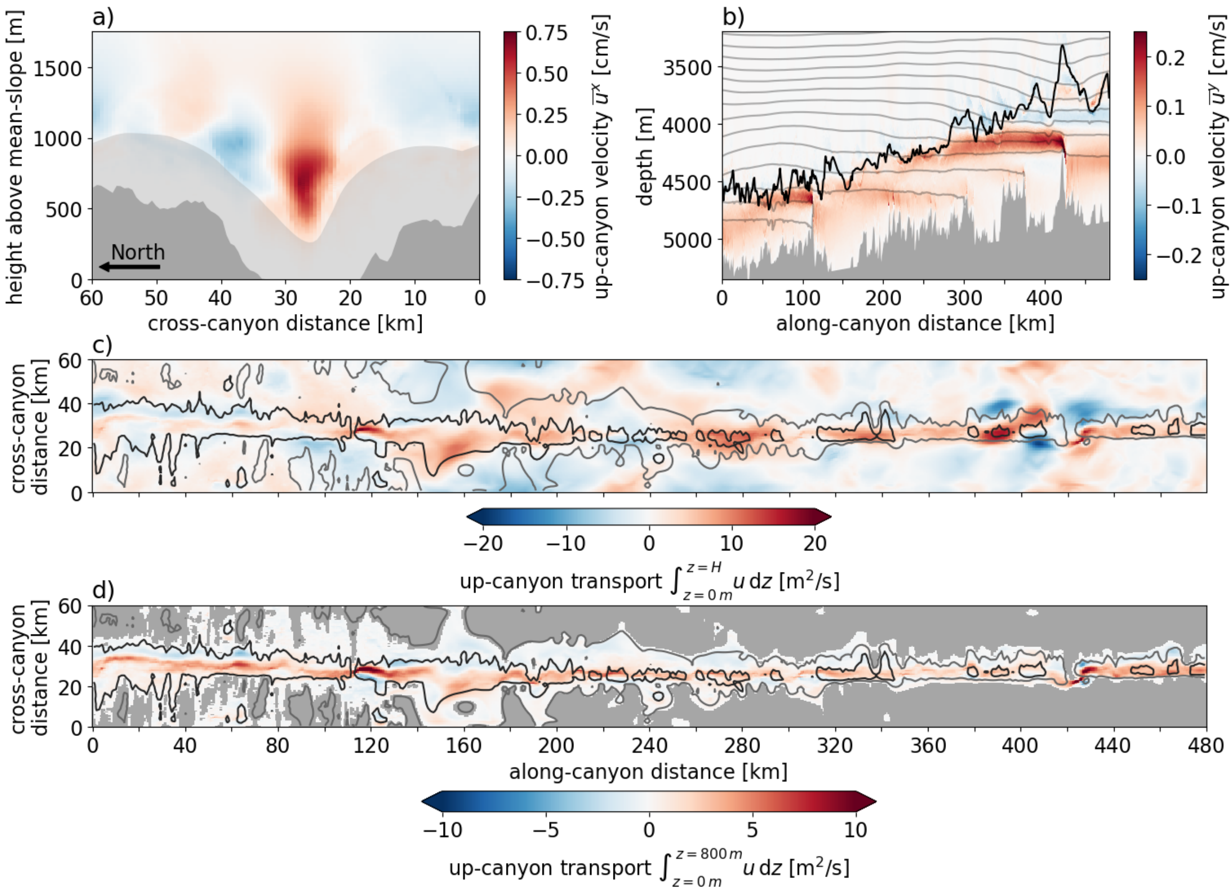

FIG. 4. Structure of up-canyon mean flow in the BBTRE Canyon. (a) Along-canyon-averaged up-canyon flow $\overline{u}^x$, with the mean canyon seafloor outlined in transparent grey shading and cross-canyon thalweg shown in the dark gray shading. (b) Cross-canyon-averaged up-canyon flow $\overline{u}^y$ in the original coordinate frame $(\hat{x}, \hat{z})$. Grey lines represent equally-spaced buoyancy surfaces. The much gentler isopycnal slopes seen in some hydrographic sections of canyons, as in Thurnherr et al. 2020, are largely an artifact of their much lower horizontal resolution, as evidenced by the favorable comparison in Figure 6. The black line marks the mean seafloor depth of the half of the domain furthest from the canyon thalweg and acts as a proxy for the crest of the canyon. (c) Up-canyon flux, integrated in the slope-normal direction z. Black and grey contours show a deep and shallow isobath, respectively, to highlight the canyon topography that shallows to the right. (d) Same as (c), but integrated only from $z = 0\,\mathrm{m}$ to $z = 800\,\mathrm{m}$ to highlight the core up-canyon jet within the canyon.

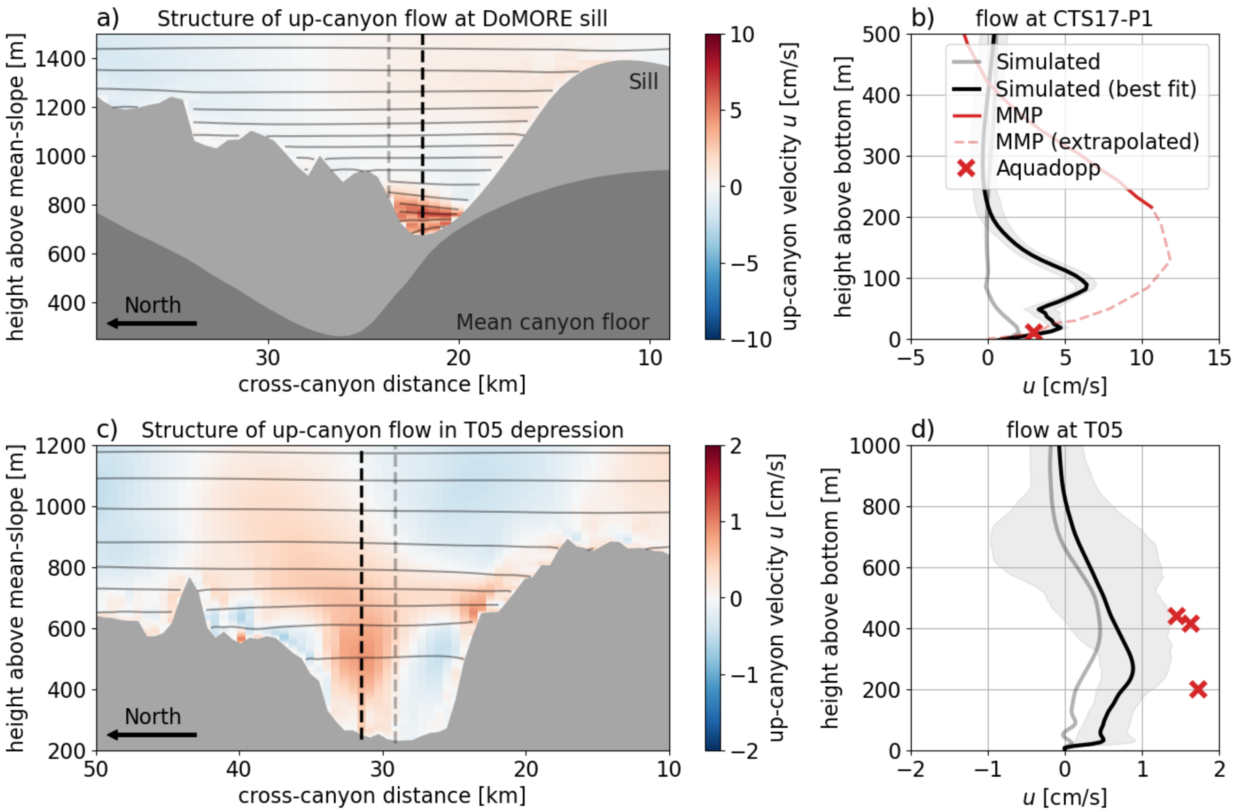

FIG. 5. Structure of up-canyon flow at two mooring sites. (a,c) Cross-canyon sections of the up-canyon flow at the locations of the DoMORE sill mooring (Clément et al. 2017) (CTS17-P1) and the BBTRE mooring Thurnherr et al. (2005) (T05). Light grey shading shows the local seafloor depth while the dark grey shading in (a) shows the mean height of the canyon floor above the mean slope, highlighting the significant vertical and cross-canyon constriction introduced by the sill. (b,d) Height-above-bottom profiles of the up-canyon flow at the locations of the two moorings (light grey lines) and shifted a few grid columns over to improve capture the core of the jet (black lines), which is somewhat displaced due to the coarse model bathymetry.

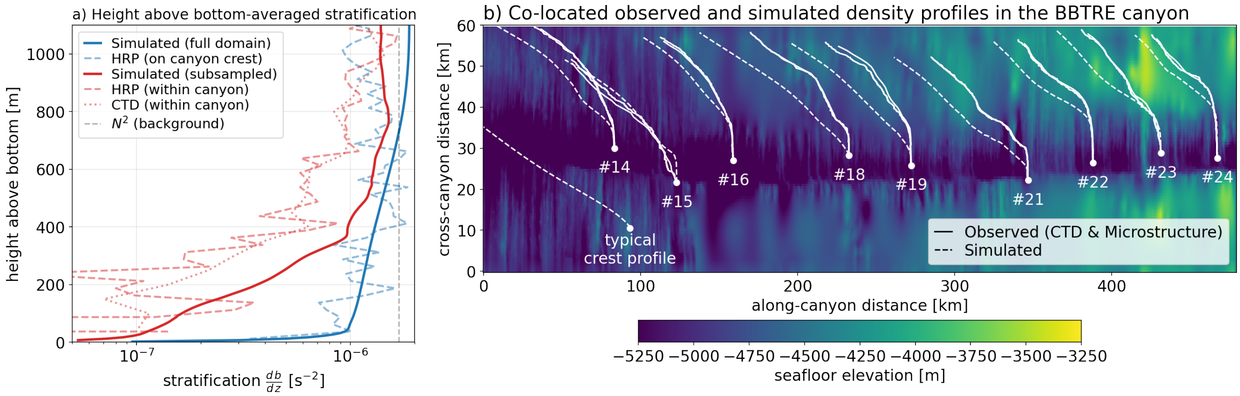

FIG. 6. Comparison between observed and simulated stratification in the BBTRE Canyon region. (a) Height above bottom-averaged profile of stratification for the full simulation domain (solid blue), for the sample-mean of nine co-located CTD casts (dotted red; Ledwell et al. 2000), free-falling HRP-microstructure profiles (dashed red; Polzin et al. 1997), and simulated CTD casts (solid red). The dashed blue line shows the sample-mean of 10 HRP profiles that follow the canyon crest just north of the domain. (b) Observed (solid) and simulated (dashed) density profiles at the nine locations sampled by the BBTRE observational campaign, overlaid on a map of the seafloor-elevation. An additional simulated profile typical of the crest region outside of the canyon is also shown, revealing an apparent sampling bias due to the strategy of measuring weakly-stratified deep depressions along the trough of the canyon in search of the released tracer (Ledwell et al. 2000).

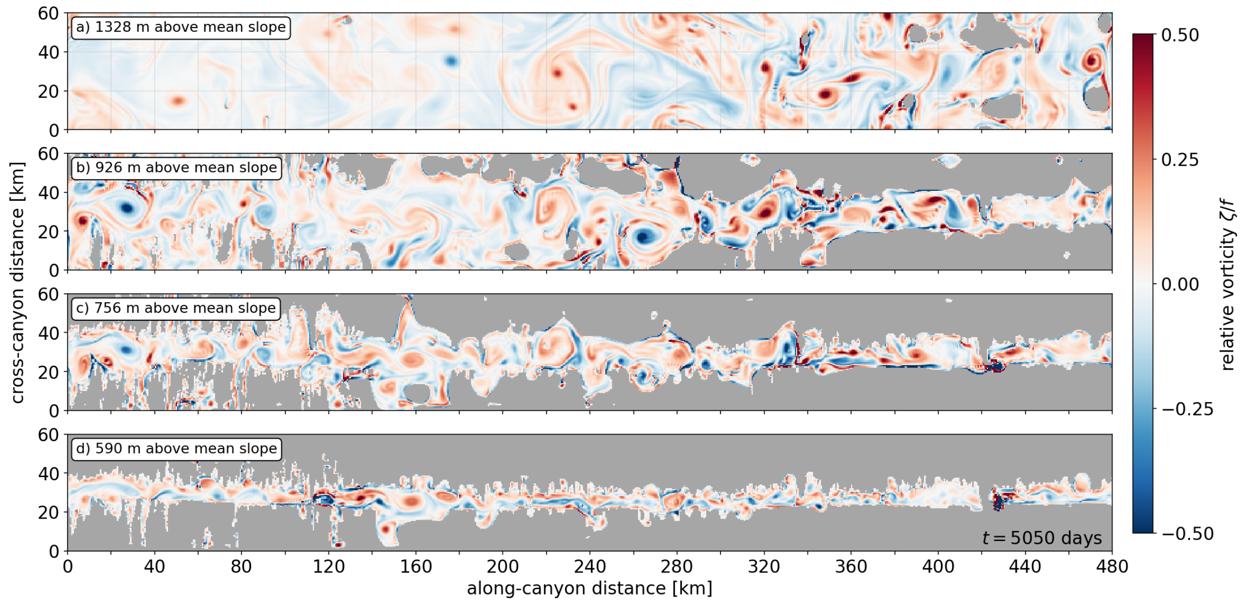

1350 FIG. 7. Instantaneous normalized relative vorticity ζ/f, or local Rossby number, in and above the BBTRE Canyon at four different heights above the mean slope, at $t = 5050$ days.

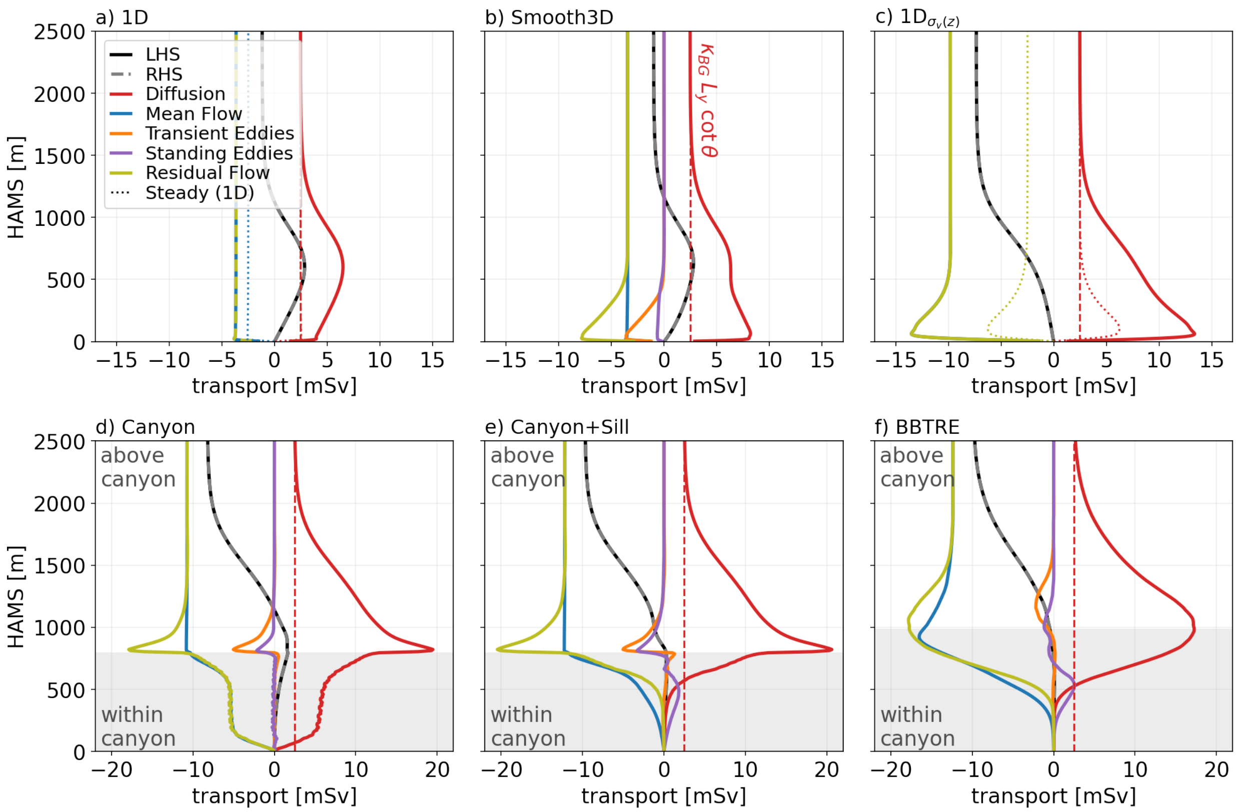

FIG. 8. Generalized integral buoyancy budget in a hierarchy of increasingly complex simulations of mixing-driven flows up a mean slope of angle θ: (a) 1D, (b) Smooth3D, (c) $1D_{\sigma_v(z)}$, (d) Canyon, (e) Canyon+Sill, (f) BBTRE. Solid lines show terms of the volume-integrated buoyancy budget (eq. 16), averaged over days 5000 to 5200, for a layer bounded by a given Height Above the Mean Slope (HAMS). We interpret the sum of the Mean Flow and Eddy terms as a Residual Flow. The left-hand-side tendencies (LHS) are equal to the remainder of the approximate balance (RHS) between slope-normal turbulent diffusion and the cross-slope residual circulation, which includes both mean and eddy components. We divide (eq. 16) by the factor $N^2 L_x \sin\theta$ to conveniently express the budget in terms of the quantity of interest, the up-slope volume transport Ψ with units of mSv $\equiv 10^3\,\mathrm{m}^3/\mathrm{s}$. Dotted lines in (a,c) show 1D steady state solutions and the dashed red line shows the integral constraint (eq. 13); in panels a and b, some of the dotted lines appear missing because they overlap with others. Grey shading shows the HAMS range spanned by the canyon, if present.

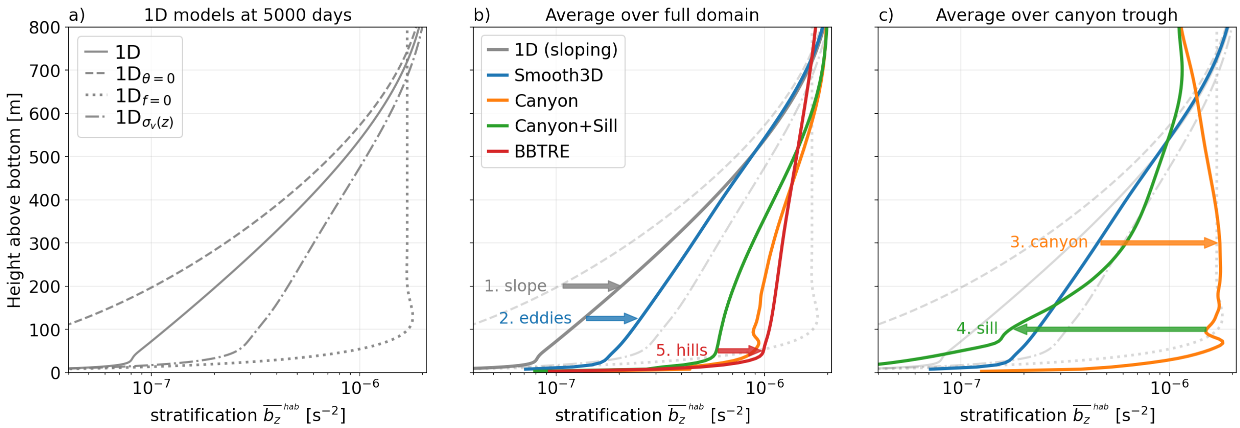

FIG. 9. Height above bottom-averaged stratification profiles at $t = 5000$ days, as a function of model complexity (lines) and domain sub-region (panels b & c). Panel (a) and grey lines in (b,c) show one-dimensional solutions: with the same parameters as the BBTRE simulations (solid); without a mean-slope ($\theta = 0$; dashed), without rotation ($f = 0$; dotted); and with an enhanced along-slope turbulent Prandtl number $\sigma_v(z)$, a crude proxy for restratification by submesoscale baroclinic eddies (dash-dotted). Colored lines show a hierarchy of three-dimensional simulations with increasingly complex topographies (see Figure 3c-f). Arrows show how the stratification profiles evolve when processes are added: 1. adding a mean-slope, 2. allowing three-dimensional eddies, 3. introducing a cross-slope canyon, 4. blocking the canyon with a sill, and 5. adding realistic hills (i.e., the BBTRE topography).

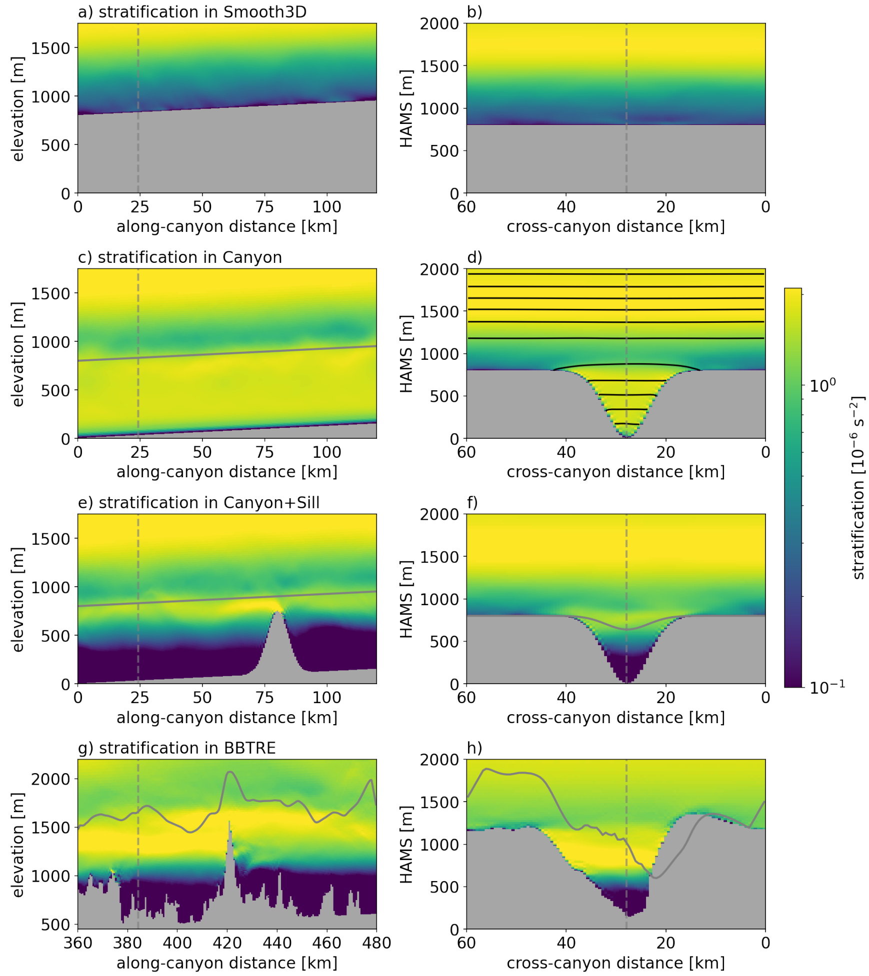

FIG. 10. Cross-slope (left) and along-slope (right) sections of the stratification along the trough of a canyon in a hierarchy of numerical simulations (Smooth3D has no canyon, so the section is arbitrary). Solid grey lines in the left column show the approximate elevation of the ridge flanks surrounding the canyon while in the right column they show HAMS of the topographic sill (if present). Dashed grey lines show the locations of the respective sections. Black lines in panel (d) represent equally-spaced buoyancy surfaces.

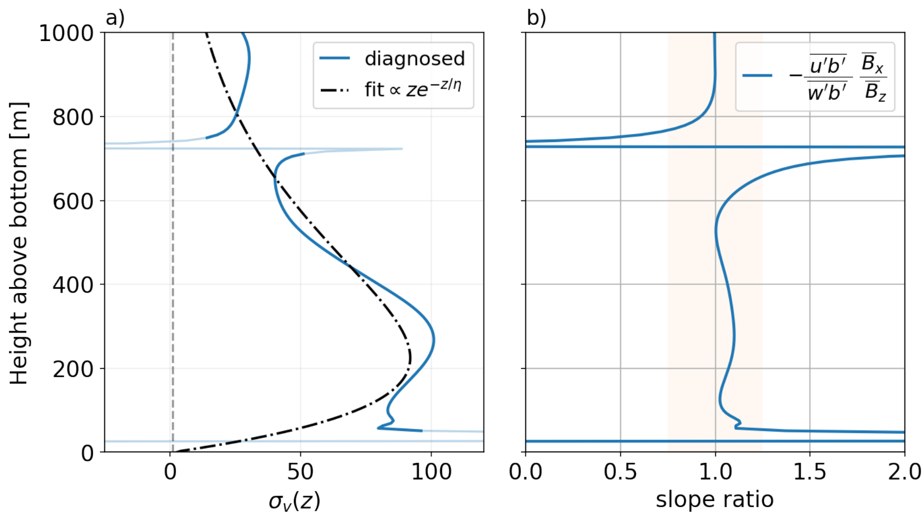

FIG. 11. a) An idealized $\sigma_v(z)$ profile (dash-dotted) with vertical scale $\eta = 225\,\text{m}$, tuned to the Smooth3D model that resolves submesoscale baroclinic instabilities using equation (A11; solid blue). b) The ratio of the mean isopycnal slope $s_b = -N^2 \sin\theta/(N^2 \cos\theta + \bar{b}_z)$ to the horizontally-averaged eddy flux slope $s = \frac{\overline{w'b'}}{\overline{u'b'}}$, which is $\mathcal{O}(1)$ outside of the strongly diabatic and frictional bottom layer. The discontinuity near 750 m is due sign reversals in both the perturbation stratification and the slope-normal eddy buoyancy flux, which enter in the denominators of expressions for σ_v and s^{-1}, respectively.